universität wien

MASTERARBEIT / MASTER'S THESIS

Titel der Masterarbeit / Title of the Master's Thesis

„Parameterizing atmospheric temperature profiles of terrestrial planets using modern machine learning regression methods“

verfasst von / submitted by

Markus Rosenberger, BSc BSc

angestrebter akademischer Grad / in partial fulfilment of the requirements for the degree of

Master of Science (MSc)

Wien, 2021 / Vienna, 2021

Studienkennzahl lt. Studienblatt / degree programme code as it appears on the student record sheet:	UA 066861
Studienrichtung lt. Studienblatt / degree programme as it appears on the student record sheet:	Masterstudium Astronomie
Betreut von / Supervisor:	Univ.-Prof. Dipl.-Phys. Dr. Manuel Güdel

Acknowledgements

I want to thank Colin Johnstone, MPhys PhD for providing me both versions of The Kompot Code, as well as all the data I needed. Thank you also for helping me at any point of this work and for all the patience you had to have with me and my questions.

Abstract

In this work, I develop and utilize an efficient method to calculate the vertical structures of the atmospheres of terrestrial planets using modern machine learning regression methods. The aim is to explore how such methods could allow us to calculate very large numbers of atmospheric profiles in a reasonable amount of time while keeping the advantages in accuracy and reliability of more detailed numerical models. This would allow us to use our most sophisticated atmospheric models to study atmospheric processes in the large number of known or soon to be known exoplanets and it would allow us to run long term evolutionary calculations for atmospheric escape.

To achieve this I use a simplified version of *The Kompot Code*, which is provided to me by Colin Johnstone. This state-of-the-art physical model can be used to model the Earth's mesosphere and thermosphere. I tune this model so that it can reproduce the basic shape of the temperature profile of the Earth's upper atmosphere. Afterwards, I use this model to calculate over 1000 atmospheric profiles in regimes similar to the modern Earth. The varying parameters are the planet's size, the CO_2 abundance in the atmosphere and the stellar XUV flux. Their exact values are chosen randomly for each simulation between well-defined lower and upper limits. I use these profiles to train and test neural networks in order to find out, which set of network parameters delivers the best results. The parameters of the neural networks are the number of hidden layers, the number of nodes per layer and the number of training epochs. To find the best combination of these parameters, I examine the ability of each network to reproduce the already known profiles.

Once this is done, I show the utility of a neural network with the best performing set of parameters according to the previous step. To do this Colin Johnstone provided me further atmospheric profiles he calculated using the full Kompot Code. They give the vertical temperature structure of the Earth's upper atmosphere during the Archean for different assumptions regarding the activity of the young Sun and the mixing ratio of CO_2 in the atmosphere. As soon as this model is trained, I am able to calculate the evolution of Earth's upper atmosphere for past eras with the input solar XUV flux and the CO_2 abundance being the only needed parameters.

In the end, I use the stellar evolution code *MORS* to calculate the temporal evolution of the emitted radiation of stars with different masses and initial rotation rates. Then I can calculate the evolution of the upper atmospheric temperature profile of a planet inside the habitable zone of these stars during its evolution using the NNs I trained before.

The result of this work is a combination of neural network parameters together with the evidence that this special arrangement is able to calculate atmospheric temperature profiles very accurately. Moreover these calculations are done very fast and can be used for planets with a wide range of properties.

Kurzfassung

Das Ziel dieser Arbeit ist es, zu zeigen, dass neurale Netzwerke sehr gut dazu in der Lage sind, vertikale Temperaturprofile der oberen Atmosphärenschichten von Planeten zu berechnen. Ein solches neurales Netzwerk kann diese Berechnungen um Größenordnungen schneller durchführen als moderne hochpräzise physikalische Modelle jeglicher Art, ohne dass dabei Genauigkeit oder Verlässlichkeit verloren gehen.

Zunächst verwende ich eine vereinfachte Version des *Kompot Codes* von Colin Johnstone. Dabei handelt es sich um ein 1D hydrodynamisches Modell für die Meso- und Thermosphäre von Planeten. Bei dieser Version müssen zunächst 2 der Eingangsvariablen, nämlich die molekulare Gasmasse sowie der Anteil des molekularen Sauerstoffs in der Atmosphäre, so definiert werden, dass das resultierende Temperaturprofil dem tatsächlichen so ähnlich wie möglich ist. Sobald das erledigt ist, definiere ich für drei weitere der Eingangsvariablen des Modells, nämlich Planetengröße, CO_2-Anteil und einfallende stellare Strahlung, Unter- und Obergrenzen. Danach berechne ich über 1000 Temperaturprofile mit immer unterschiedlichen zufälligen Werten für jede der drei Variablen zwischen den definierten Grenzen. Diesen Datensatz teile ich dann auf in einen Trainings- und einen Testdatensatz. Mit ersterem kalibriere ich neurale Netzwerke auf einem breiten Gitter an Eigenschaften, wobei diese Eigenschaften die Anzahl der Schichten des Netzwerkes, die Anzahl der Neuronen in jeder Schicht sowie die Anzahl der Trainingsepochen sind. Den Testdatensatz verwende ich, um die Ergebnisse der trainierten Netzwerke zu validieren. MSE und RMSE dienen dabei als Maßzahlen für die Performance der Netzwerke.

Im nächsten Schritt verwende ich dieses Modell gemeinsam mit einem Satz an Temperaturprofilen berechnet von Colin Johnstone mit der Vollversion des Kompot Codes. Diese Profile wurden unter der Annahme Strahlungsinputs der jungen Sonne zur Zeit des Archaikums auf der Erde, also zu einer Zeit zwischen 4.0 und 2.5 Mrd. Jahren in der Vergangenheit, berechnet. Außerdem wurde ein breiter Bereich an Werten für den CO_2-Anteil in der Atmosphäre angenommen. Diesen Datensatz teile ich ebenfalls in Trainings- und Testprofile ein. Diesmal allerdings vertraue ich auf die Ergebnisse von zuvor und verwende nur noch das oben abgeleitete Modell.

Zuletzt verwende ich noch ein Modell zur Berechnung von Sternentwicklungen namens MORS, um Strahlungsprofile für Sterne unterschiedlicher Rotationsgeschwindigkeiten und Massen zu erhalten. Die Ergebnisse verwende ich dann als Input für das zuvor trainierte neurale Netzwerk, um Temperaturprofile der oberen Atmosphärenschichten eines Planeten in der habitablen Zone dieser Sterne zu berechnen.

Am Ende dieser Arbeit soll also ein Aufbau eines neuralen Netzwerkes stehen, der äußerst schnell, aber dennoch genau und zuverlässig, die Temperatur in den oberen Schichten der Atmosphäre von Planeten unterschiedlichster Eigenschaften berechnen kann.

Contents

List of Tables

List of Figures

1 Introduction

While mankind needed thousands of years until the eight planets of the Solar System were found, the process of discovering new planets outside of the solar neighbourhood, so-called exoplanets, and determining their properties is a lot faster now. The first exoplanet was detected almost 30 years ago. Since then, more than 4700 further ones have been discovered (exoplanet TEAM, 2021). Their properties exceed by far what was previously known from the Solar System. Their masses range from less than that of the Earth to more than ten times the mass of Jupiter and they orbit different types of stars with orbital periods ranging from days to decades.

To illustrate the wide range of parameters for discovered exoplanets, I show in Fig. 1.1 the orbital distances against planetary mass for more than 4500 confirmed exoplanets, with the green cross showing the Earth for comparison. Marker colors show the effective temperatures of the host stars, with black indicating that the temperature of the star is not known. The data I used is available online at the NASA exoplanet archive [1]. Currently the orbital distances of the confirmed exoplanets range from approximately 0.004 AU to more than 7500 AU, while the already known planetary masses cover a range from 0.02 $M_\oplus$ up to the theoretical mass limit of a planet. This limit is set to approximately 13 $M_{Jup} \approx 4134\ M_\oplus$ (Chabrier and Baraffe, 2000). Bodies with higher masses already burn deuterium in their core and are called Brown Dwarfs. Fig. 1.1 also shows that the majority of currently known exoplanets is located much closer to their host star than the Earth's separation from the Sun. Moreover most of them also have much higher masses. High-mass planets located very close to their host stars are called *Hot Jupiters*. The strong representation of Hot Jupiters in our sample of detected exoplanets is most likely due to observational biases because high mass planets with small orbital distances can be found much easier with today's methods than small planets or those with larger orbital distances.

While the planetary and atmospheric parameters of known exoplanets themselves span a large range, the situation is even more complex because the basic properties of the stars that they orbit are also highly diverse. The effective temperatures of planetary host stars range from only 575 K to 57,000 K and the vast majority of values are between approximately 4000 K and 8000 K. Stars also differ significantly in their emission of X-ray and extreme ultraviolet (EUV) radiation, and in their winds and these parameters evolve in complex ways. This leads to an innumerable amount of possible parameter combinations and each individual combination leads to a planet with unique properties. One can guess that not only is it hard to derive the properties of one single planet but it is much more elaborate to get the properties of all of them. Though in most cases it is

[1] `https://exoplanetarchive.ipac.caltech.edu/`

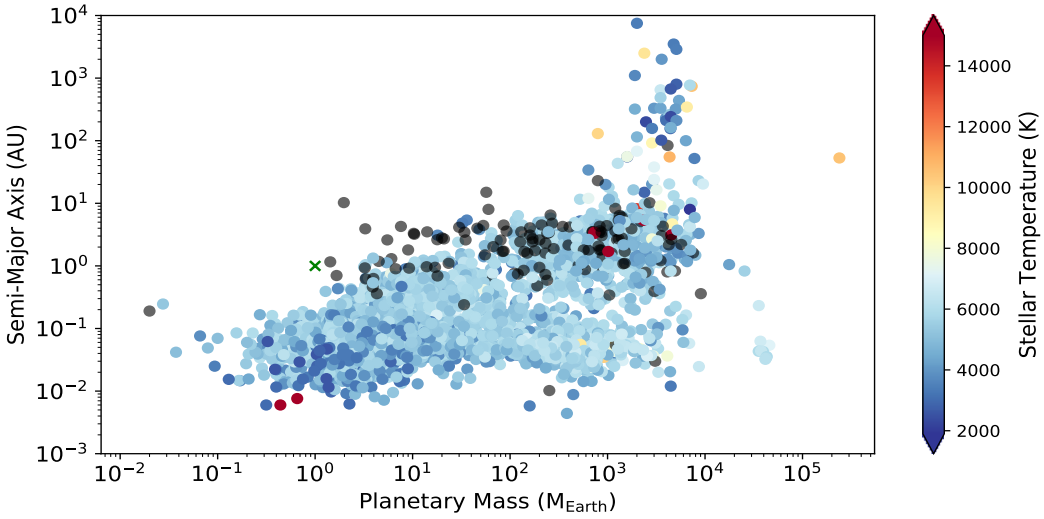

Figure 1.1: Semi-major axis in AU against mass in Earth masses of more than 4500 currently confirmed exoplanets. The marker color represents the temperature of the host star. Black dots indicate stars with currently unknown effective temperatures. Note the wide range of possible values for each of the parameters. Today's Earth is represented by the green cross.

possible to measure the basic parameters like size and orbital distance of those planets, it is much harder to learn anything about their atmospheres.

More than a decade ago, the Hubble and Spitzer Space Telescopes enabled scientists to take a look into atmospheres of Hot Jupiters and it was even possible to reveal the existence of several different chemical species inside these envelopes (Eggenberger and Udry, 2010). Only a few years later, Tsiaras et al. (2016) detected the first atmosphere of the super-Earth 55 Cancri e. This exoplanet has a mass of approximately 8 $M_\oplus$ and its atmosphere consists mainly of hydrogen and helium and no evidence of water vapor was found (Tsiaras et al., 2016). It did not last very long until water vapour was also found in an atmosphere of another super-Earth K2-18 b (Tsiaras et al., 2019). In both cases, a chemical model was used additionally to derive the abundances of several chemical species, or at least their possible border values, in the observed atmospheres.

Possibly the most interesting chemical species to look for in the atmospheres of exoplanets are molecular hydrogen (H_2), nitrogen (N_2) and oxygen (O_2) as well as water vapour (H_2O) and carbon dioxide (CO_2). Their exact abundances can make the difference if a planet is habitable or not. Of course, this is only valid if the planet is inside the habitable zone (HZ) of its parent star and has already lost its primordial H/He atmosphere. This is the atmosphere a planet gathers right after its formation from the circumstellar disk that orbits the planet's host star. Stökl et al. (2015) stated that a planet that grows to a mass of > 0.1 $M_\oplus$ before the circumstellar disk of the system dissipates can accumulate a protoatmosphere dominated by hydrogen and helium. The mass of the core influences the amount of gas that is collected as well as the timescale on which it is lost again with

higher core masses capturing more gas and also keeping it for a longer time. Lammer et al. (2014) derived that bodies with masses above about 1 $M_\oplus$ can keep their envelopes for their entire lives though this depends on the details of the host star's activity evolution (Johnstone et al., 2015).

Traditionally, the HZ of a star is "defined as the circumstellar region in which a terrestrial-mass planet with a CO_2-H_2O-N_2 atmosphere can sustain liquid water on its surface" (Kopparapu et al., 2013). Owen and Mohanty (2016) stated that even if a terrestrial planet is inside the HZ of an M dwarf or a solar-type star, there is no chance of habitability if it has an H/He atmosphere with a mass fraction of the order of a few percent of the planet's mass. This is because hydrogen is a very powerful greenhouse gas, which would lead to pressure and temperature conditions at the planet's surface that do not allow water to be liquid (de Wit et al., 2018).

Nakazawa et al. (1985) simulated the conditions on Earth during its evolution when the primordial atmosphere was still present. They derived that the temperature at the bottom of the primordial atmosphere was at least two times higher than the hypothetical surface temperature of the early Earth if there would have been no H/He envelope. This effect is called thermal blanketing. Temperatures at the bottom of the atmosphere were probably higher than 2000 K, depending on the grain opacity factor, the effective accretion time and the density of the solar nebula, i.e. the gaseous cloud around the Sun, which was present during the formation of the Solar System. This would lead to the fact that Earth's surface material was almost completely molten at that time. The pressures at the bottom of the envelope were calculated to be as high as 1000 times the surface pressure of the modern Earth, again dependent on the three previously mentioned parameters. According to Wolfgang and Lopez (2015), a rocky Earth-like core is very likely to have a primordial H/He atmosphere of about 1% of the planets mass. Therefore, for a planet to be habitable it is very important that it loses this primordial envelope during its evolution to build a secondary atmosphere by the release of various volatile species from different planetary reservoirs like the mantle and the ocean. This can happen due to a number of processes; for example an impact during the growth phase or tectonic related activity (Noack et al., 2014).

These secondary atmospheres can be mixtures of various molecules. For example the atmosphere of Venus consists mainly of CO_2 (ca. 96.5%) and N_2 (ca. 3.5%). Further components are noble gases and many other components with mixing ratios in the range of several parts per million (Basilevsky and Head, 2003). In comparison, the atmosphere of modern Earth consists mainly of N_2 (ca. 78%) and O_2 (ca. 21%) and a lot of further components with rather small abundances. Although Earth and Venus may be very similar in terms of radius, mass and insolation (the solar radiation intensity Venus receives is only a factor of 1.9 higher than what Earth receives), the conditions on the surface are very different. Basilevsky and Head (2003) state that, on average, the surface temperature on Venus is about 740 K, compared to approximately 288 K on Earth's surface. Moreover the surface pressure is more than 90 times higher on Venus than it is on Earth. These huge differences between the early Earth, Venus and modern Earth show that the composition of the atmosphere is very important for the conditions at the planet's surface. In addition to the composition, also the amount of atmosphere is very important. For example Mars

and Venus have very similar atmospheric compositions, but the mass and density of the Venus atmosphere is much higher, which leads to way higher temperatures on Venus (in addition to the fact that the orbital distance of Mars is a lot bigger) [2].

Most atmospheric loss processes occur in the upper layers of the atmosphere and are mainly caused by the parent star's high-energy radiation and winds (Johnstone, 2021). They can be split up into thermal and non-thermal processes. An example of a thermal process is Jeans escape, which takes place at and above the exobase where the gas density becomes low enough that the gas is non-collisional. Particle speeds at the exobase approximately follow a Maxwellian distribution and some particles in the tail of this distribution have upward speeds that exceed the escape velocity meaning they can leave the planet (Catling and Zahnle, 2009). It is mostly important for low mass particles like hydrogen but has to be considered for higher mass particles in hot atmospheres too. An example of a non-thermal escape process is the removal of atmospheric particles in the exosphere by the host star's wind (Kislyakova et al., 2014). Another non-thermal process, among many others, is the loss of hot particles created in photochemical reactions (Amerstorfer et al., 2017); this process is also driven by stellar high-energy radiation which is responsible for driving the chemistry that leads to such reactions. Either ways, the host star's X-ray and ultraviolet radiation is very important for investigations of loss processes and thus the evolution of the star and the atmosphere of the planet are closely linked (Johnstone et al., 2019). In general, hotter atmospheres show higher loss rates due to either several enhanced loss processes like Jeans escape or a more expanded envelope, which is thus more exposed to the stellar wind.

The chemical structure also plays a major role when it comes to loss processes since, as I already mentioned, lower mass particles can escape more easily than heavier ones. This can be shown considering the pressure scale height kT/mg. In this term k represents the Boltzmann constant, T is the temperature, m the molecular mass of the gas and g is the gravitational acceleration (Johnstone, 2021). In a hydrostatic atmosphere, the pressure scale height denotes the distance at which the pressure decreases by a factor of 1/e. If a gas is made of heavier particles, i.e. has a higher m, the pressure scale height is lower so the atmosphere is less expanded. A lighter gas means a more expanded atmosphere and therefore more rapid losses. Another important factor is the planet's intrinsic magnetic field. Although the magnetosphere prevents particles from being ionized and swept away by the stellar wind, it also transports energy from the wind into the lower atmosphere, where it accelerates particles and thus drives another escape process. Gunell et al. (2018) found out that in fact the mass escape rate from today's Earth is even higher than it is from an unmagnetised Earth-like planet.

I already mentioned a broad range of external processes that influence the structure and composition of a planet's atmosphere. Of course, there are also further factors that are very important for its properties. In addition to the stellar radiation input, also the planet's mass and the chemical composition of the atmosphere are crucially important for the structure of the upper atmosphere. Using Earth as an example, the upper atmosphere starts above the stratopause, at an altitude of approximately 50 km above the surface,

[2] `https://nssdc.gsfc.nasa.gov/planetary/factsheet/`

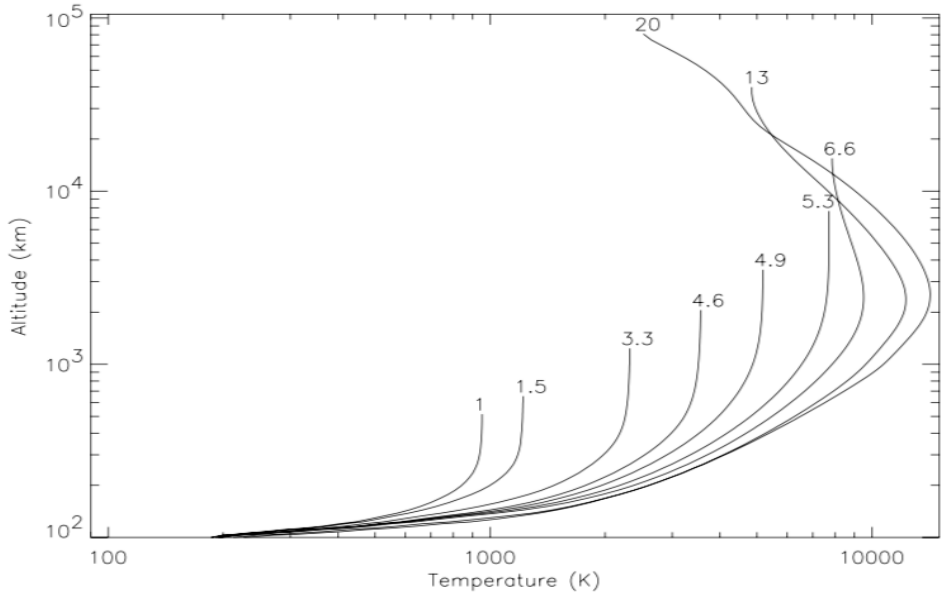

Figure 1.2: Temperature profiles of the thermosphere considering different values of the solar extreme UV input normalized to an approximated value of modern Sun of 5.1 erg s^{-1} cm^{-2} (Fig. 6 of Tian et al. (2008)).

and can be split into several different layers. The layer up to an altitude of about 100 km is called mesosphere and is characterized by a negative temperature gradient, i.e. temperature is decreasing with increasing altitude, due to cooling by CO_2 molecules, which emit infrared radiation to space. Above the mesosphere, the temperature gradient becomes positive again, which is where the thermosphere starts. There the temperature increases with height since particles like O and O_2 absorb the Sun's X-ray, extreme and far UV radiation. At the top of the thermosphere, at an altitude of a few hundred km and where the gas is approximately non-collisional, there is the exobase. The exact height of the exobase and the temperature throughout the thermosphere are mostly defined by the Sun's activity. Tian et al. (2008) calculated temperature profiles of the upper atmosphere up to the exobase dependent on the stellar extreme UV input. Fig. 1.2 shows Fig. 6 of Tian et al. (2008) where each curve represents a level of extreme UV input normalized to a present day solar value of approximately 5.1 erg s^{-1} cm^{-2}. Both the exobase height and temperature increase with higher radiation input until about 5 times the present value. Beyond this point, the exobase altitude still increases but the exobase temperature decreases again because adiabatic cooling becomes more and more significant (Tian et al., 2008). This is because of the expansion of the atmosphere due to the efficient escape of major atmospheric components (Tian, 2013).

The chemical structure of the atmosphere can be divided into two important layers: the homosphere and the heterosphere. The homosphere is where the mixing-ratios of long-lived molecules like N_2, O_2 and CO_2 are almost constant with height, which is between the Earth's surface and an altitude of approximately 120 km. In the overlying heterosphere the

species are separated by their masses because of molecular diffusion causing the mixing ratios of heavier molecules to decrease with increasing altitude. Moreover, the solar radiation dissociates the molecules, so that atomic O and N dominate the thermosphere. The mesosphere and the thermosphere also coincide with another layer of the atmosphere called the ionosphere, where the ionization of particles due to X-ray and EUV radiation leads to there being a significant population of ions and electrons (Johnstone, 2021).

During its evolution, a stars radiation spectrum changes a lot and these changes depend sensitively on the star's basic parameters like mass and (initial) rotation rate. Figs. 1.3a and 1.3b show the differences of the X-ray luminosity evolution between a solar mass star and one with $M_* = 0.5\ M_\odot$ up to an age of 5 Gyr. In both diagrams, the blue, green and red lines represent fast, medium and slow initial rotators, respectively. Faster rotation rates go together with higher X-ray emission rates. One can also see that the higher mass star emits more X-ray luminosity at the same age. However, because the HZ of lower mass stars is at smaller orbital distances, a planet inside the HZ of a $0.5\ M_\odot$ star receives a lot more X-ray radiation during its lifetime than a planet inside the HZ of a solar mass star. Fig. 1.3c shows the mass evolution of the hydrogen dominated atmosphere of a $0.5\ M_\oplus$ planet, which orbits a solar mass star at a distance of 1 AU. The initial mass of the atmosphere is assumed to be $5 \times 10^{-3}\ M_\oplus$. The line colors represent the initial rotation rates of the planet's host star and are defined as before. It can be seen that a planet loses its entire atmosphere after 100 Myr if it orbits a fast rotating star, while it is able to keep about 45% of its envelope until an age of 5 Gyr if the parent star is a slow rotator. The same correlation is also shown in Johnstone et al. (2015) and Kubyshkina et al. (2019). Although these calculations may be simplified a lot, they still show that the stellar mass and initial rotation rate are very crucial for the evolution of an atmosphere of a planet around this star.

Since observations of atmospheres of exoplanets are biased due to observational constraints and therefore not accessible in most cases, modelling atmospheres plays a major role in research. But models are not only important for exoplanets, they are also widely used to find out more about both the history and the future of the atmospheres of planets within the Solar System. However, one large drawback of very sophisticated models is that they need a lot of computational effort and quite a long time for a single simulation. Reconsidering the number of already confirmed planets (and also the number of those that will be detected in the future) together with the wide range of possible parameters, like mass and orbital distance, and also the different properties of the host stars, it is impossible to simulate every single atmosphere in detail. Faster and more efficient methods are needed to gather information about planetary atmospheres.

On the other hand, neural networks are known to deliver very good results in a variety of scientific applications like cancer diagnosis (Bottaci et al., 1997) or face recognition. Peek et al. (2020) show a small overview of current application fields of neural networks in astronomy and they also mention the main advantage of neural networks, which is the fact that they are significantly faster than full models while showing comparable results in terms of accuracy if enough training data is available.

The aim of my work is to show the ability of modern machine learning regression methods to reproduce vertical temperature profiles for upper atmospheres given only the

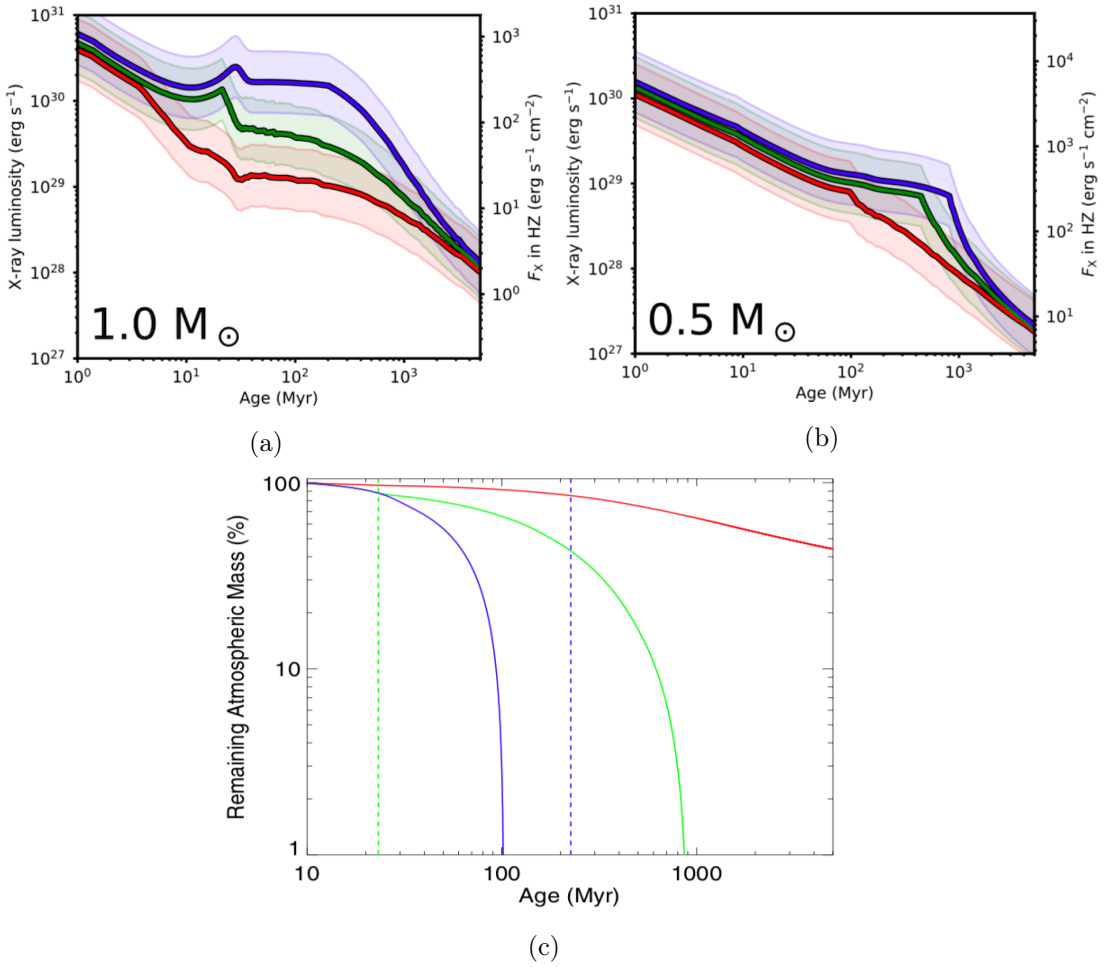

Figure 1.3: (a) & (b) Evolution of stellar X-ray luminosity for fast, medium and slow rotators (blue, green and red lines, respectively) assuming different masses of the star (from Fig. 11 of Johnstone et al. (2020)). (c) Mass reduction of a hydrogen dominated atmosphere with an initial mass of 5×10^{-3} $M_\oplus$ of a 0.5 $M_\oplus$ planet around a solar mass star at an orbital distance of 1 AU. The line colors are the same as in (a) & (b). Vertical dashed lines represent the saturation times of the star (Fig. 4 of Tu et al. (2015)).

values of a few input parameters. To achieve this, at first I have to tune a simplified version of The Kompot Code so that it is able to calculate Earth's upper atmospheric temperature profile properly. Afterwards I have to generate a training and a test data set and find a proper setup for my neural network. I also test the performance of this specific setup by comparing its output to vertical temperature structures calculated by Johnstone et al. (2021) using the full Kompot Code for the atmosphere of the Earth during the Archean. In the end, I use the model I derived and trained previously to investigate the evolution of the temperature profile in the meso- and thermosphere of a planet in the HZ of stars with different masses and initial rotation rates.

2 A demonstration of neural networks

In this chapter I am going to show how I proceed from generating vertical temperature profiles with a state-of-the-art hydrodynamic model for upper atmospheres to using them to train a neural network. I will also show that the results of a simplified and thus also much faster version of the code are accurate enough to use them as training profiles. Since a lot of profiles are needed for the training process I define a grid of three input parameters, i.e. the planet size, the CO_2 mixing ratio and the stellar XUV input [1]. On this parameter grid I run more than 1000 simulations with the simplified code to create the temperature profiles for both training and testing of the neural network. At the end of this chapter I will describe how I find the best setup of hyper-parameters for my neural network.

2.1 Atmospheric model

Johnstone et al. (2018) presented a possibility to simulate upper atmospheres of arbitrary planets: The Kompot Code. This is a first principles 1D hydrodynamic model using only a few basic planetary and stellar variables as input. It covers physical processes like radiation transfer through the atmosphere and infrared cooling as well as energy exchange between the neutral, ion, and electron gases. It also includes 63 chemical species (vertical profiles of some of them are shown in Fig. 2.1) with 503 chemical reactions and physical processes like heat conduction, diffusion, the expansion or contraction of the atmosphere due to temperature or composition changes and many more. Because of this wide range of covered processes, The Kompot Code takes quite a long time for one simulation. Sometimes, it needs several days until the simulated atmosphere reaches a steady state. Fig. 2.2 shows the molecular mass of the gas and the total XUV flux used in the full Kompot Code as well as the output profiles of temperature and density throughout the simulation grid for the case of modern Earth.

In order to reduce the time per simulation while keeping as much accuracy as possible, the main author of Johnstone et al. (2018) simplified The Kompot Code and created The Kompot Code v2. This simplified version covers way less chemical processes and assumes that the atmosphere is hydrostatic. Moreover, the XUV radiation transport is simplified a lot by assuming that all photons have the same energy and that all chemical species have a single absorption cross-section. Concerning the heating process this model assumes that a fixed fraction of the energy in the XUV field is absorbed instead of calculating the full set of physical processes. On the other hand, only cooling by CO_2 molecules is possible and only atomic oxygen can excite these CO_2 molecules because this is also

[1] XUV is short for X-ray, extreme UV and far UV radiation, i.e. a wavelength range from 1–400 nm.

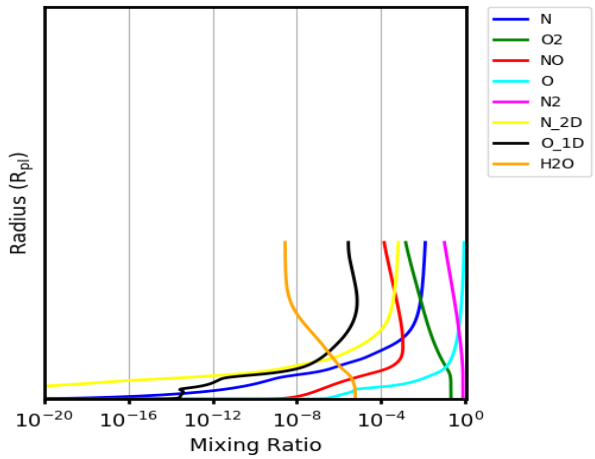

Figure 2.1: Vertical profiles of the most abundant chemical species from a simulation of the modern Earth using the full Kompot Code.

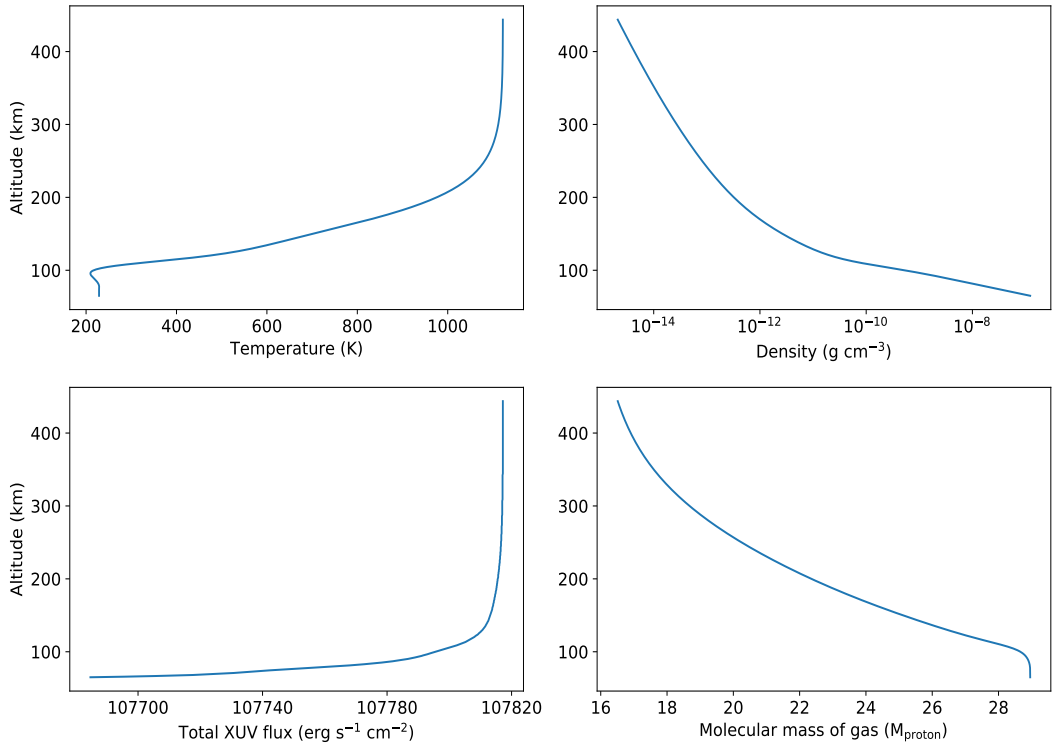

Figure 2.2: Vertical profiles of four basic quantities from the full Kompot Code for the case of modern Earth. The upper panels show the output of temperature and density at the end of the simulation. The lower panels show the input profiles of the solar XUV radiation and the molecular mass of the gas.

the main process in the Earth's atmosphere. Thermal conduction is implemented quite similar to the full version of the Kompot Code. The only difference is that the code does not calculate the conductivity from the chemical composition because of the simplified chemistry.

Just as the full Kompot Code the simplified version needs some planetary and stellar variables as input. Firstly, the mass and radius of the planet. It also needs the density and the temperature of the gas at the base of the simulation domain and the XUV flux coming from the host star on top of the atmosphere. The altitude of the base and the top of the simulation domain and the number of grid cells in between as well as the mixing ratio of CO_2 are also needed as input parameters. Furthermore, there are a few free parameters to vary in order to improve the performance of the model. Two of these free parameters are the molecular mass of the gas m_{gas} and the atomic oxygen mixing ratio f_{O}. So at the very beginning I need to tune these two parameters in a way that the simplified Kompot Code can reproduce the basic shape of the temperature profile of the Earth's upper atmosphere.

2.1.1 Fitting m_{gas} and f_O

As I already mentioned before, I have to define the two parameters m_{gas} and f_{O} such that I can reproduce the "real" temperature profile, which was calculated using the full Kompot Code, as good as possible. Of course, there will be deviations between the recreated and the original profile because of all the simplifications. One of them applies to the chemistry which leads to the fact that both quantities m_{gas} and f_{O} are now set as constants throughout the whole simulation grid. As Fig. 2.2 shows in the full Kompot Code m_{gas} decreases towards higher altitudes from almost 29 $\mathrm{M_{proton}}$ at the base of the simulation grid, where gas is molecular, to about 16.5 $\mathrm{M_{proton}}$, corresponding to atomic gas, at the top. Fig. 2.1 shows the vertical profiles of the mixing ratio of 8 chemical species used in the full Kompot Code. The mixing ratio of oxygen varies from about 10^{-7} at the bottom to close to 1 at the top of the domain. From these two figures I can get a good first guess on the most probable value ranges for both quantities.

As I already mentioned there are several planetary and stellar parameters, which I need as input for the simplified Kompot Code. For a simulation of modern Earth I simply set mass and radius of the planet to 1 $\mathrm{M_\oplus}$ and 1 $\mathrm{R_\oplus}$, respectively. The exact altitude of the lower and upper border of the simulation domain is arbitrary to some extent, but I choose them to be 50 km and 500 km above the planet's surface. These altitudes include the Earth's mesosphere and thermosphere and the top of the simulation domain is approximately located at the Earth's exobase. Above this level the atmosphere becomes nearly isothermal. The domain is split up into 100 grid cells. For temperature and density of the gas, T = 267 K and N = 2.441×10^{16} $\mathrm{cm^{-3}}$ show good results. I estimated the solar XUV flux to be about 3.95 erg $\mathrm{s^{-1}}$ $\mathrm{cm^{-2}}$, according to Ribas et al. (2005). For the mixing ratio of CO_2 I assume a typical value of 4×10^{-4}, so 0.04% of the gas. All input parameters and their chosen values are summarized in Tab. 2.1.

To find proper values for m_{gas} and f_{O} I define a grid for each parameter. Therefore, I expand the value ranges mentioned above a little bit leading to the following ranges:

Table 2.1: Input parameters of the model and their specific values for simulating Earth's atmosphere.

Name	Value	Description
M_{pl}	1.0 $\mathrm{M}_{\oplus}$	mass of the planet
R_{pl}	1.0 $\mathrm{R}_{\oplus}$	radius of the planet
T_{base}	267.0 K	temperature of gas at base of simulation domain
N_{base}	2.441×10^{16} cm^{-3}	density of gas at base of simulation domain
$F_{\mathrm{xuv,in}}$	3.95 erg s^{-1} cm^{-2}	stellar XUV flux at top of simulation domain
z_{min}	50 km	altitude of base of simulation domain
z_{max}	500 km	altitude of top of simulation domain
$f_{\mathrm{CO_2}}$	4×10^{-4}	mixing ratio of CO_2
m_{gas}	*to be fitted*	molecular mass of gas
f_{O}	*to be fitted*	mixing ratio of O

- $10\ M_{\mathrm{proton}} \leqslant m_{\mathrm{gas}} \leqslant 35\ M_{\mathrm{proton}}$
- $1 \times 10^{-11} \leqslant f_{\mathrm{O}} \leqslant 1 \times 10^{-1}$

Starting with these border values I make my grid smaller and smaller until I find the best fitting values for both parameters. In order to restrict the size of the grid I compare every temperature profile calculated using the simplified Kompot Code with the standard profile shown in the upper left panel of Fig. 2.2 and look for combinations of m_{gas} and f_{O} where the sum of squared temperature differences has a minimum. Since the two models run on different grids, I calculate the difference between their respective outputs at 17 altitudes throughout the whole grid.

The contour plot in Fig. 2.3 shows the sum of squared temperature differences for one of the grids. The area with the darkest blue shading shows the parameter combinations which lead to the smallest deviations. It corresponds to values for m_{gas} between approximately 21.5 M_{proton} and 22 M_{proton} and for $f_{\mathrm{O}} < 1\times\ 10^{-7}$. Fig. 2.3 also shows that there seem to be no changes in the goodness of the fits for $f_{\mathrm{O}} < 1 \times 10^{-9}$. In fact, the temperature and density profiles do not change anymore for such small oxygen abundances compared to $f_{\mathrm{O}} = 1 \times 10^{-9}$. Therefore I cut off the grid at this point. To restrict the remaining parameter pairs even more I calculate the relative temperature difference ΔT_{rel} at the exobase between every model and the standard profile.

$$\Delta T_{\mathrm{rel}} = \frac{T_{\mathrm{mod}} - T_{\mathrm{standard}}}{T_{\mathrm{standard}}} \tag{2.1}$$

where T_{mod} and T_{standard} are the exobase temperatures of the profiles calculated with the simplified and the full Kompot Code, respectively. Each model with $\Delta T_{\mathrm{rel}} < 0.5\%$ is marked with a cross in Fig. 2.3. Concerning these conditions, I can find a best fitting pair of values for m_{gas} and f_{O}. Within the regions corresponding to the smallest sums of squared deviations only four grid points show sufficiently small values for ΔT_{rel}. The

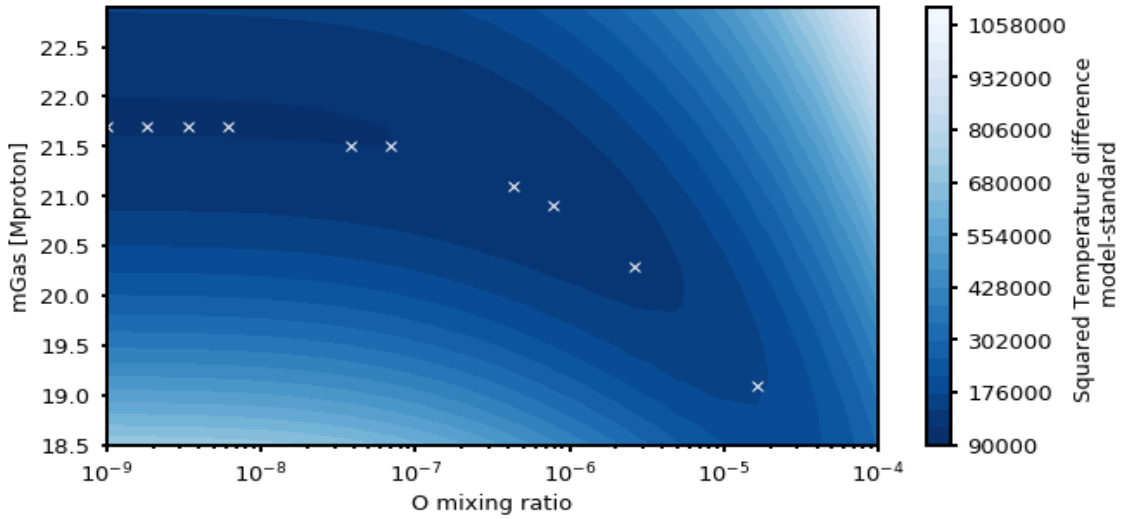

Figure 2.3: Sum of squared temperature differences between simulations and standard profile as contours. Crosses show models with $\Delta T_{\mathrm{rel}} < 0.5\%$ at the exobase.

minimum of these four values is $\Delta T_{\mathrm{rel}} \approx 0.17\%$ and belongs to the same model run as the second smallest of all sums of squared temperature differences. The pair of parameters

$$m_{\mathrm{gas,best}} = 21.7\ M_{\mathrm{proton}}$$
$$f_{\mathrm{O,best}} = 1 \times 10^{-9}$$

belonging to this specific simulation should lead to a temperature profile as close as possible to the standard profile, which was calculated using the full Kompot Code.

Running a simulation with the simplified Kompot Code using the input parameters from Tab. 2.1 together with the two parameters I just derived, yields the density and temperature profiles shown in Fig. 2.4 (orange curves in both diagrams). Both are not a perfect fit of the standard profiles but taking into account all the simplifications which were made, together with the fact that the calculation only needed less than two minutes (compared to several days for the full model), at least the reproduction of the temperature profile is sufficient. The main feature which I was not able to reproduce with the simplified code is the temperature minimum at an altitude of approximately 100 km. The models which show this temperature minimum more accurately have a vertical offset and thus also show large errors. Additionally, if I try to improve the fit of the density profile, the fit of the temperature profile gets worse. It seems that the vertically constant values of many input parameters as well as the simplified chemistry lead to the fact that the density profile cannot be reproduced much better. Or at least that the temperature profile is useless in simulations leading to more accurate density profiles. But since I am only using temperature profiles to train neural networks in my work I neglect the resulting errors in the density profiles and focused on finding the

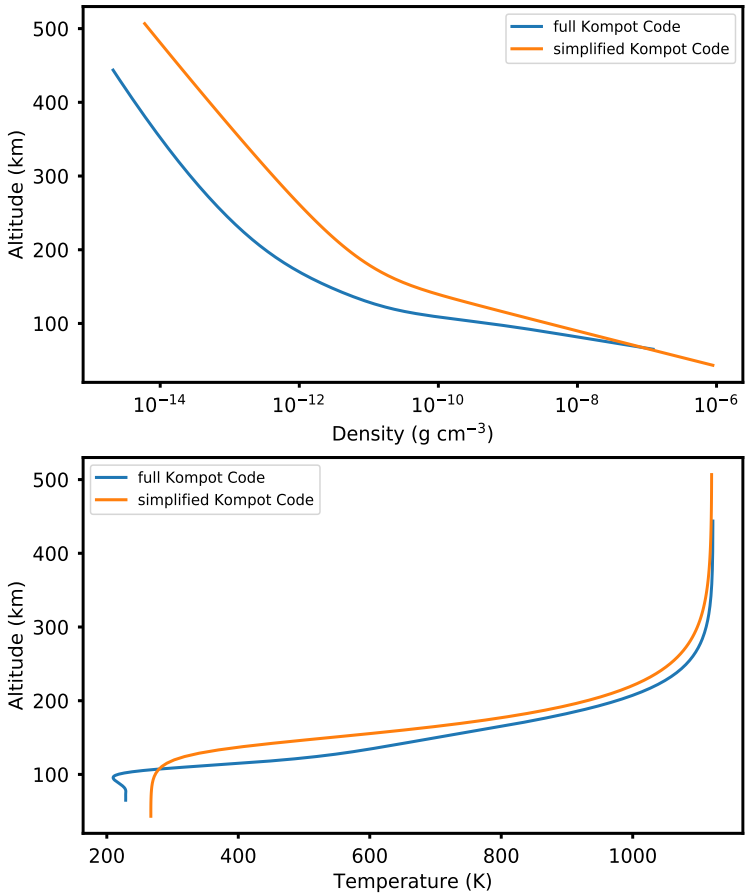

Figure 2.4: Density and Temperature profiles using the best fitting values for $m_{\mathrm{gas}} = 21.7\ \mathrm{M}_{\mathrm{proton}}$ and $f_{\mathrm{O}} = 1 \times 10^{-9}$ (orange) compared to the reference profiles calculated with the full Kompot Code (blue).

most accurate temperature structure. Fig. 2.4 shows that although there are quite a lot of simplifications in the second version of The Kompot Code, it is still very useful to calculate the properties of planetary atmospheres. Moreover, it can do it a lot faster with an accuracy good enough to use the profiles for the training of my neural network.

2.2 Grid of models

In the previous section I showed that the simplified Kompot Code can reproduce the standard temperature profile of Earth's upper atmosphere quite well. Thus, now I use this model to calculate vertical temperature profiles on a grid of the three input parameters I mentioned in the beginning of this chapter: planet size, CO_2 mixing ratio and stellar XUV radiation input. I choose these three parameters because Johnstone (2021) stated that

they are very crucial for many thermal and chemical processes in the upper atmosphere and therefore also for its structure.

Since I put the focus of my work on terrestrial planets and so far there is no uniform classification scheme for exoplanets, I define the upper mass limit for my simulations to be 10 $M_\oplus$. According to Tuomi et al. (2019) this is a planet size for which solid surfaces are at least likely to occur. The lower mass limit is to some extent arbitrary and I choose it to be 0.4 $M_\oplus$ which is in between the masses of Mars and Venus. Of course together with the mass of the planet also its radius has to change. In my simulations I assume a fixed density for each planet which equals the density of the modern Earth $\rho_\oplus = 5510$ kg m^{-3}. Then I calculate the radius of the planet using:

$$R_\mathrm{pl} = \left(\frac{3M_\mathrm{pl}}{4\pi\rho_\oplus}\right)^{\frac{1}{3}} \tag{2.2}$$

In the following, I am going to refer to the size of the planet as its mass only, keeping in mind that the radius of the planet is also changed implicitly.

In 2019 the average CO_2 abundance at Earth's surface was 408.9 ± 0.1 ppm (Dunn et al., 2020) corresponding to 0.04% of the global atmosphere near the surface. And according to Qian et al. (2017) CO_2 is well-mixed up to about 80–90 km, which is where the CO_2 homopause is located and well above the base of my simulation domain. Above this level its abundance decreases exponentially. Therefore and in order to also consider atmospheres with higher CO_2 mixing ratios, I use values between 1×10^{-4} and 1×10^{-3} in my simulations.

Concerning the stellar XUV radiation the value I used for the Earth case shown in the previous section was 3.95 erg s^{-1} cm^{-2}. According to Ribas et al. (2005) the solar high-energy flux between 0.1 nm and 120 nm of the Sun was up to 6 times the present value in the last 3.5 Gyr. Therefore to account for younger or more active stars as well as for smaller distances between the host star and the planet than in the case of modern Earth, I choose the upper limit of the XUV flux to be 100 erg s^{-1} cm^{-2}.

In summary, the grid on which I run my simulations has the following limits:

- **Planet size:** $0.4\ \mathrm{M}_\oplus \leqslant M_\mathrm{pl} \leqslant 10.0\ \mathrm{M}_\oplus$ and R_pl in a way that the planet's density equals the terrestrial value of $\rho_\oplus = 5510$ kg m^{-3}.
- **Carbon dioxide mixing ratio:** $1 \times 10^{-4} \leqslant f_{\mathrm{CO}_2} \leqslant 1 \times 10^{-3}$
- **Stellar XUV input:** $1\ \mathrm{erg\ s^{-1}\ cm^{-2}} \leqslant F_\mathrm{xuv,in} \leqslant 100\ \mathrm{erg\ s^{-1}\ cm^{-2}}$

For the remaining input parameters I choose the same values as I used in Sect. 2.1.1. In total, I simulate 512 atmospheres using a set of random values for each quantity within these given ranges. From each simulation I get a vertical temperature structure to train my neural network. To test it afterwards, I calculate just as many test profiles in the same way. Each profile consists of temperature values on 104 vertical levels equally distributed between 43.25 km and 506.75 km above the surface of the planet.

Although the three input variables span large ranges of possible values the shape of the temperature structure looks quite similar for most of the simulated atmospheres. It is

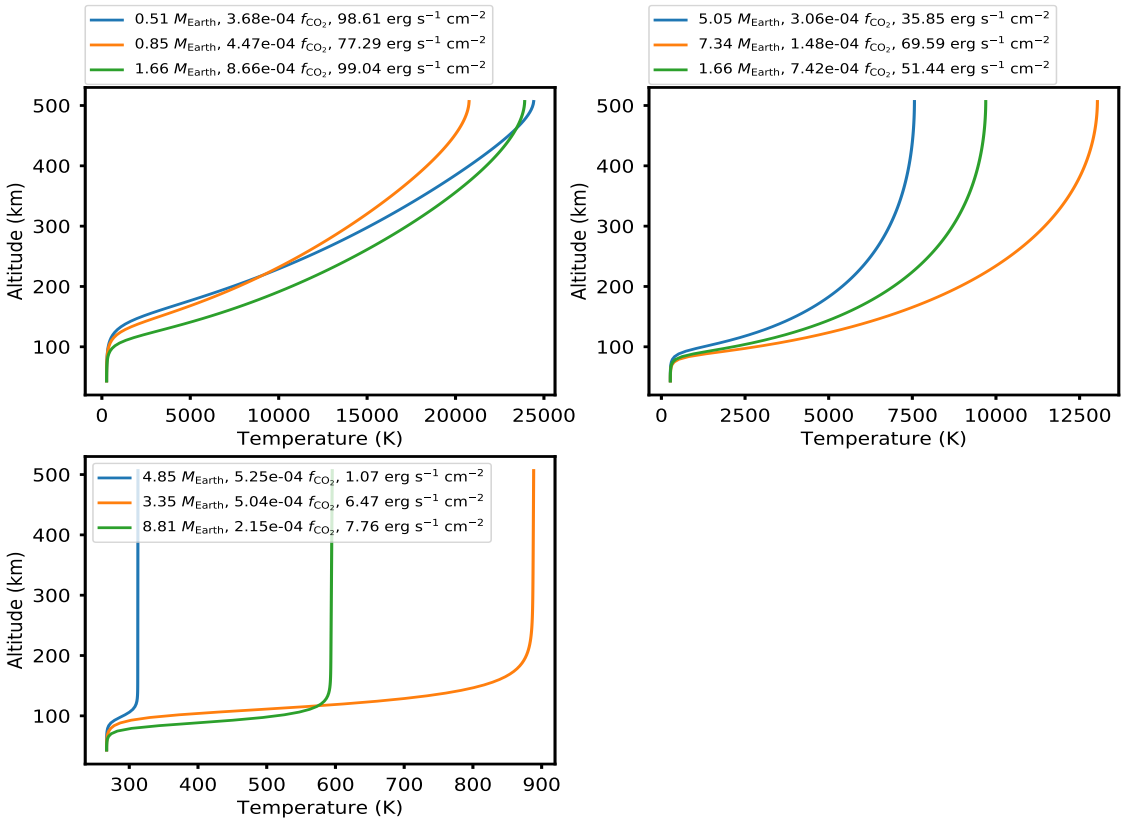

Figure 2.5: Temperature profiles from the test data set showing some of the hottest (upper left panel) as well of some of the coldest (lower left panel) planet set ups. The upper right panel shows planets with medium temperatures at the exobase. The legends give for each profile the mass of the planet, the CO_2 abundance and the stellar XUV input of the respective simulation.

basically the shape of the vertical profile which I calculated using the simplified Kompot Code (Fig. 2.4). This is at least partially caused by the fixed temperature at the base of the simulation domain. Fig. 2.5 shows 9 profiles I calculated. The legends show the values of the three input parameters planet mass, CO_2 mixing ratio and stellar XUV input for each simulation. Although the base temperature of each simulation is fixed to 267 K the temperature at the exobase, i.e. the top of the simulation domain, varies between 300 K (lower left panel) and almost 25,000 K (upper left panel). The upper right panel shows atmospheres with medium exobase temperatures. However, "medium" here refers to the temperature range I got in my simulations since these "medium" values are still about 10 times higher than the temperatures of the modern Earth case.

In Fig. 2.6 the temperature at the top of the simulation domain is shown in two different diagrams dependent on two of the three input variables for each diagram. Red dots represent the highest and blue dots the lowest temperatures. In the left panel there

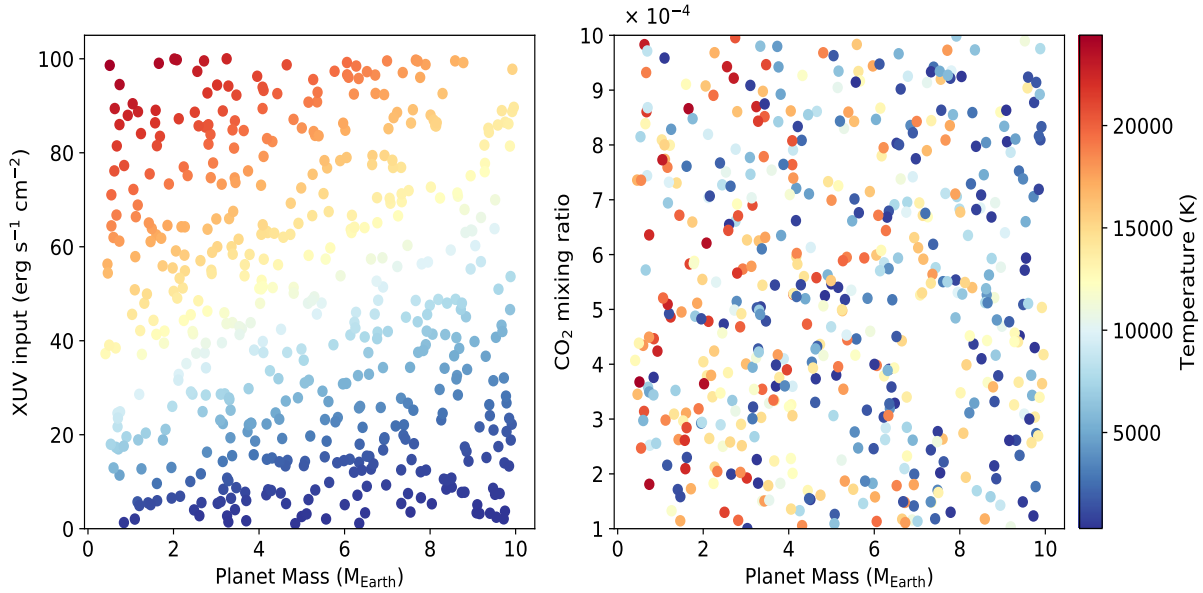

Figure 2.6: Temperatures at the top of the simulation domain for all 512 test profiles. Higher temperatures at the exobase are shown with red colours, while blue colours represent lower temperatures.

is clearly a structure visible. If small planets receive large amounts of XUV radiation they develop the highest exobase temperatures occurring in my data set (upper left corner), while the top of the atmosphere of a large planet is colder if it receives only a small stellar XUV input flux (lower right corner). In the right panel there does not seem to be any correlation between the temperature and the CO_2 mixing ratio. Both, red and blue dots, occur over the whole grid of possible CO_2 mixing ratios. The relations between the exobase temperature and the three input variables are also visible in Fig. 2.5. All three simulations in the upper left panel have very high XUV radiation inputs and rather small planet masses, while the lower left plot consists of simulations of large planets receiving way less radiation. However, the exact shape of the profile seems to be determined by a combination of all three input parameters.

2.3 Training of the neural network

Although the simplified Kompot Code calculates the vertical temperature structures a lot faster than the full model with only small inaccuracies, my aim is to run even more simulations in even less time using modern machine learning regression methods. In my work I use *Keras* (Chollet et al., 2015) based upon the open source platform *TensorFlow* (Abadi et al., 2015) to create, train and test such a model. This model will be able to calculate temperature profiles in a reasonable amount of time while keeping the advantages of accuracy and reliability of more detailed numerical models. The background of such

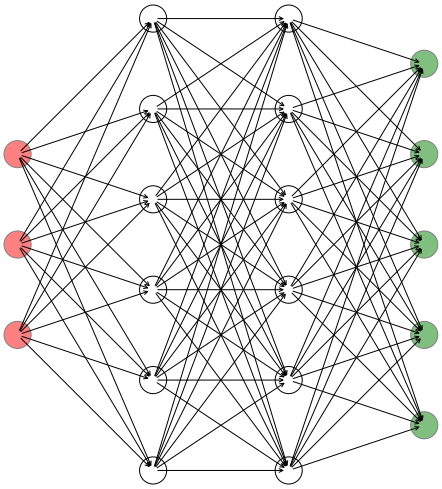

(a)

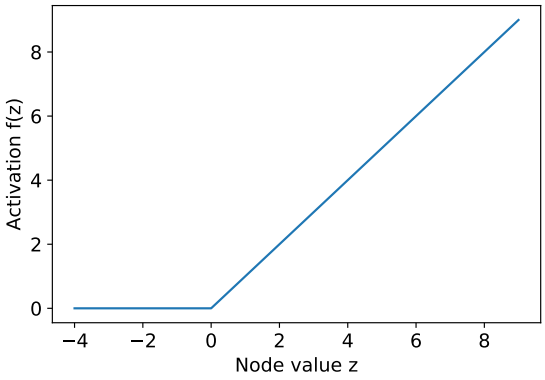

(b)

Figure 2.7: (a) A simplified scheme of a neural network consisting of an input layer with three neurons, two hidden layers with six neurons each and one output layer with five neurons. (b) A sketch of the ReLU activation function, which I use in my work.

a neural network and how to use it is described in Nielsen (2015). I only give a short summary here:

A neural network (NN) consists of several layers and each layer itself consists of neurons, which I also call nodes in my work. In Fig. 2.7a each circle corresponds to one node and each column of circles represents one layer. The first column with the red circles stands for the input layer while the last one with the green circles represents the output layer. The two layers in between are so-called hidden layers. Since this is only a simplified scheme, the actual number of neurons in each layer is much higher in most real applications. The connections between all the layers, which are shown as arrows here, are the outputs of the nodes in one layer used as the input for the nodes in the next one. Each node in every layer, except for those in the input layer, has its own set of weights w_i and a bias b. Here i represents the index of each node in the previous layer. Given an input x_i (which would be a vector with three entries when transferring from the input layer to the first hidden layer and a vector with six entries if it was the input of the second hidden layer or the output layer of the sketch in Fig. 2.7a) of a node the value of this node is given by

$$z = b + \sum_i w_i \cdot x_i \tag{2.3}$$

However, z is not the output of the node yet. The actual output of the neuron, the activation value, can be calculated in many different ways. Nielsen (2015) mostly uses the sigmoid activation function $\sigma(z)$, which transforms z into a value between 0 and 1. But

since the Rectified Linear Unit (ReLU) is "the most successful and widely-used activation function" (Ramachandran et al., 2017) I use it in this work. The ReLU function is shown in Fig. 2.7b and is defined as

$$f(z) = max(0, z) \tag{2.4}$$

The activation value $f(z)$ of each node in one layer is then merged into the input x_i for every node in the following layer. All these transfers between the layers are represented by the arrows in Fig. 2.7a.

In the case of my NN the input layer consists of three nodes, one for each input parameter, and the output layer consists of 104 nodes, one for each altitude of the temperature profiles. The number of hidden layers I use and the number of neurons in each of them is still to determine. How I do this will be shown in the following section. Before I start the training process all the weights and biases in the whole NN are just random numbers. But when I start to train my NN, i.e. I assign every neuron in the first layer with a specific value of my input parameters, the network calculates the activation values in the first hidden layer in the way I described before. Then it transfers them to the next hidden layer, again calculates all the activation values and so on for each hidden layer in the network until it finally reaches the output layer. There the activation value of every node is compared to the temperature in the respective altitude of the training profile I use. Of course, the differences between each pair of values should be as small as possible in the end. Therefore, I have to define a loss function and I simply use the mean squared error (MSE) here. After it calculated the MSE of one step of the training process the network tries to adjust the weights and biases in each node of every layer so that the MSE decreases. This is done by an optimization algorithm. In my work I use the *Adam* algorithm, which is "an algorithm for first-order gradient-based optimization of stochastic objective functions" (Kingma and Ba, 2017). This means it computes the first-order derivatives of the loss function and tries to change all the variables, in this case the weights and biases of every single neuron in the whole network (except for the input layer, since these neurons do not have any weights and biases), in a way that the loss function becomes as small as possible. Of course, this minimum will not be found after a few steps. This is why a large number of training epochs and many training profiles are necessary.

2.3.1 The grid of networks

When it comes to defining the setup of a neural network there are three main parameters: the number of hidden layers, the number of nodes in each layer and the number of epochs I train the NN. These parameters are also called hyper-parameters. Since there is no a priori combination of these values to use I have to find the best setup myself. Similarly to the fitting process I did in Sect. 2.1.1, I define a parameter grid to set up many different models and investigate their performances, a process that is called cross-validation. Although I mentioned before that it takes a lot of training epochs to find the minimum of the MSE, it is not as easy as "the more training, the better are the results". Because if the NN is trained for too long with the same data it kind of gets

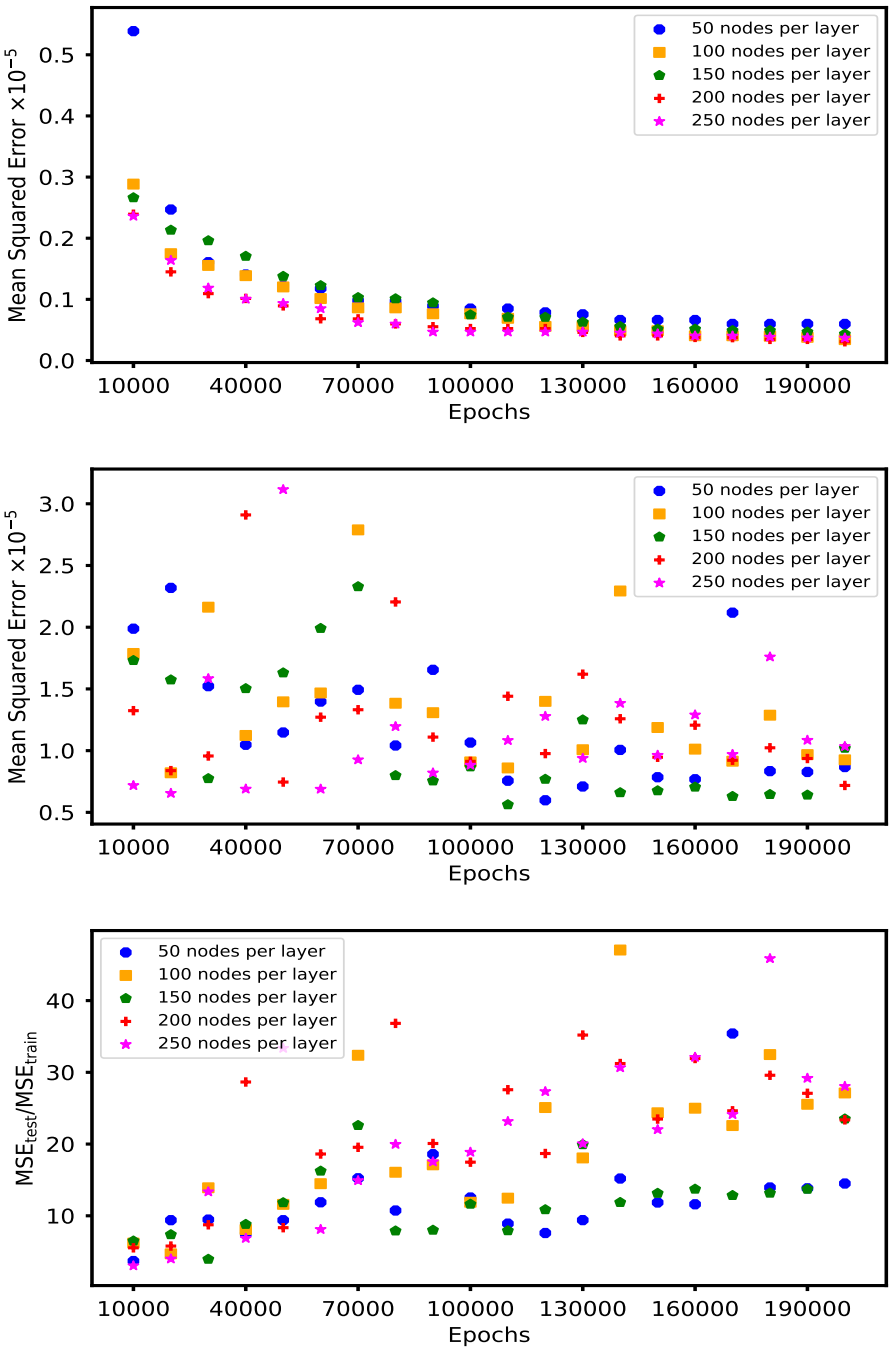

Figure 2.8: *Upper and middle panel:* Mean squared error of all models with 4 hidden layers as a function of nodes per layer and number of training epochs for the training and the test process, respectively. *Lower panel:* Ratio of MSEs of the test and training processes.

used to it, i.e. the model learns specific patterns from the training data that cannot be generalized, which leads to errors when the model needs to reproduce previously unknown profiles. This is called overfitting. Therefore I try a lot of different numbers of training epochs and I also have to check the performance of the model on the test data periodically to see if the model overfits the training data already. This is how I define the parameter grid:

- **Number of layers:** 1, 2, 3, 4
- **Number of nodes per layer:** 50, 100, 150, 200, 250
- **Number of training epochs:** Up to 200,000 epochs with a checkpoint frequency of 10,000 epochs

This means that I train 20 different models for up to 200,000 epochs. Every time when 10,000 training epochs are done, I check the smallest MSE of the training process up to this point as well as the current MSE of the test process. The upper and middle panel in Fig. 2.8 show these two quantities of all the models with four hidden layers during the whole process of training. As supposed, the mean squared error of the training process becomes smaller with more epochs done. On the other hand the MSE of the test data does not show any similar structure. For example the test MSE of the model with 4 hidden layers and 150 nodes per layer, represented by the green pentagons, shows the smallest MSE after 30,000 epochs, reaches then quite high values until 70,000 epochs and afterwards the error again is a lot smaller during the remaining process. Similar fluctuations are also visible for all the other models with 4 hidden layers. In the lower panel of Fig. 2.8 the ratio of test and training mean squared errors for each model at every checkpoint is shown. Very large values in this diagram show where overfitting of the training data may be an issue. In such cases the training MSE is very low already but the test MSE stays at higher values or is even increasing. Of course, it is desirable that the network performs well on the training and the test data but also that both MSEs do not differ too much.

2.4 Results

To find a proper setup for my NN I have to check all three panels I show in Fig. 2.8 for every number of hidden layers in the grid. In the following I use only those with 4 hidden layers as an example for the process of cross-validation:

In the first panel the differences of the errors are less than 3×10^{-6} K^2, which is already very good. So this does not restrict the value ranges of the hyper-parameters a lot. But the lower panel shows that the error ratio is small for all models if they were trained for less than 20,000 epochs. The smallest error ratios occur for the model with 250 nodes per layer, represented by magenta stars at around 10,000 or 20,000 training epochs. If I continue to train the same NN for a total of 30,000 epochs, the test MSE increases by a factor of 2–3. Therefore, I train the same setup again for a maximum of 30,000 epochs

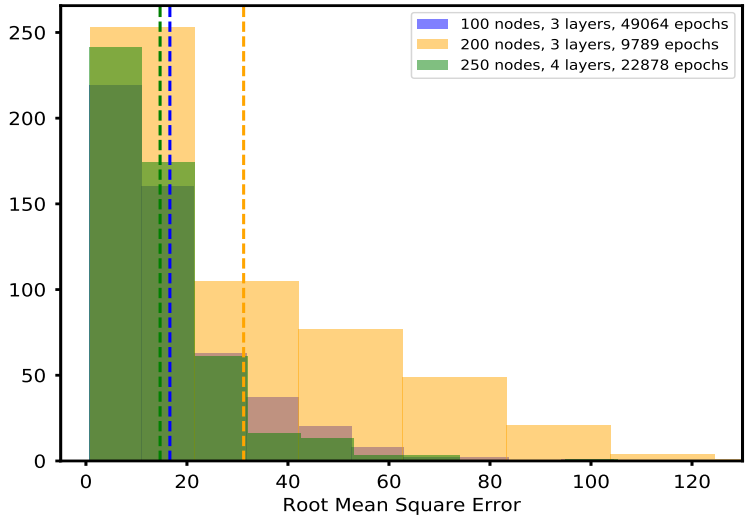

Figure 2.9: Comparison of the three best models so far showing the RMSE as a histogram for all test profiles. The dashed lines are the respective mean values. *Note:* Model 2 has three root mean square errors >130 K. They are not shown in this plot.

to look at which point the training MSE has its minimum. This comes out to be after 22,878 epochs.

I do the same process with all networks with 1, 2 and 3 hidden layers. But those with 1 and 2 hidden layer show test errors five or ten times the errors of models with 3 and 4 layers. This is why the other two very good performing models are one with 3 layers, 100 nodes each and trained for 49,064 epochs and another one with 3 layers but 200 nodes each and only trained for 9789 epochs. The reason why the three setups are quite different from each other is the complexity of such a NN with thousands of weights and hundreds of biases. So at a first approach, I have reduced the number of possible setups of my NN from 20 to the following 3:

- **Model 1:** 3 hidden layers, 100 nodes, 49,064 training epochs
- **Model 2:** 3 hidden layers, 200 nodes, 9789 training epochs
- **Model 3:** 4 hidden layers, 250 nodes, 22,878 training epochs

Now I have to compare these three networks to find the best one. To do this, I reproduce more than 500 test profiles with every model and calculate the root mean square error (RMSE) between the output of the NN and each profile calculated with the simplified Kompot Code. Fig. 2.9 shows the RMSE of each model as a histogram with the vertical dashed lines as the respective mean values. It shows that model 1 and model 3 are very close to each other but the latter performs a little bit better. Therefore, the NN I use in

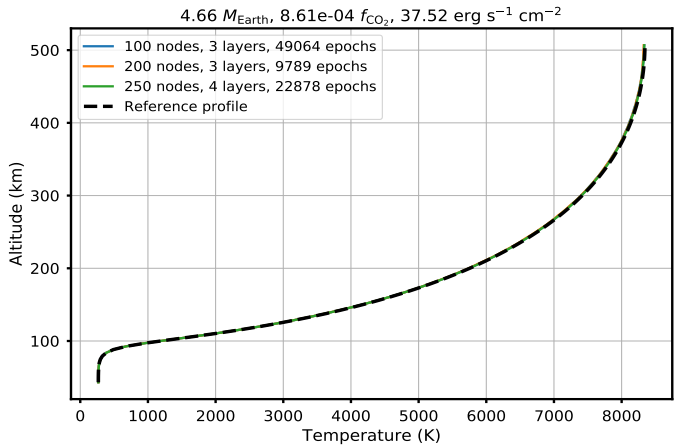

(a)

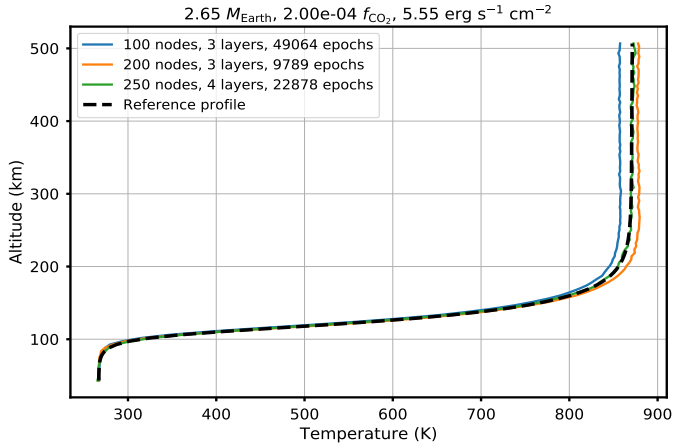

(b)

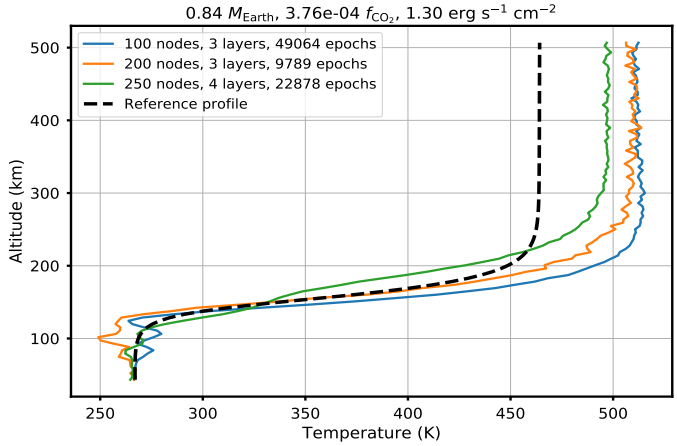

(c)

Figure 2.10: The output of the three NNs I considered to perform the best compared to the corresponding temperature profiles I calculated using the simplified Kompot Code (*Reference profiles*).

the next step of my work will consist of 4 hidden layers with 250 nodes per layer and it is trained for 22,878 epochs. The mean RMSE of this model over all test profiles is only ca. 14.7 K, the median is even smaller. I consider this as a very good result since the time per simulation is a lot smaller than it is when using any of the two Kompot Code versions.

Fig. 2.10 shows a comparison of three different temperature profiles from the test data set (dashed line) with the respective outputs of models 1–3. All three models were capable to reproduce many profiles almost perfectly. An example for this case can be seen in Fig. 2.10a. Fig. 2.10b shows an example where the best model still performs very good, while the other two show some inaccuracies. But there are also some parameter combinations where not even the best model can calculate the vertical temperature structure correctly (see Fig. 2.10c). Although the deviations may look very big in this case the maximum error of the predicted temperature profile is less than 50 K, which is not that much after all. Actually it can be a bit misleading, if I only take a look at the RMSE of a single simulation to evaluate its goodness. For example, model 1 has an RMSE of about 10.2 K in Fig. 2.10a but only 1.7 K in Fig. 2.10b, although the reference profile seems to be fitted better in the first one. The higher RMSE in the first panel is simply the result of the ten times higher exobase temperature. In Fig. 2.10c the RMSE of model 1 is only about twice as much as in the first diagram although there are quite large deviations between the reference profile and the NN output. Therefore, I also have to consider the exobase temperature together with the RMSE.

Fig. 2.11 shows the errors of all available test profiles for two of the three input parameters in each diagram. The left column shows the RMSE while the right column shows the RMSE normalized to the temperature at the exobase of the respective simulation. Since this is the most error-prone part of the profiles calculated with the NNs, I use the temperature at the top of the reference profile. The marker area represents the error magnitude and its color the atmospheric temperature at the top of the simulation domain. The first two diagrams in the left column are very similar to those in Fig. 2.6. In addition to before, now I show that simulations with higher temperatures at the exobase, i.e. red dots, also seem to have larger root mean square errors. The lower left plot confirms this. Although large errors are also possible in simulations with low exobase temperatures, they occur there less often. However, as the right column shows and as I already mentioned before, this does not mean that my NN performs better on profiles with lower temperatures. In fact, the relative RMSE is way higher for atmospheres with low exobase temperatures. For example, the maximum relative RMSE appears for the simulation with $M_{\mathrm{pl}} \approx 0.84\ \mathrm{M}_{\oplus}$, $f_{\mathrm{CO_2}} \approx 3.76 \times 10^{-4}$ and $F_{\mathrm{xuv,in}} \approx 1.3$ erg s^{-1} cm^{-2} ($\mathrm{RMSE_{rel}} \approx 5.7\%$). The exobase temperature of this simulation is only about 464 K. On the other hand, the simulation with the smallest relative RMSE has input values $M_{\mathrm{pl}} \approx 2.12\ \mathrm{M}_{\oplus}$, $f_{\mathrm{CO_2}} \approx 4.78 \times 10^{-4}$ and $F_{\mathrm{xuv,in}} \approx 87.2$ erg s^{-1} cm^{-2}, leading to a relative RMSE of less than 0.02%. This setup leads to an exobase temperature of more than 21,400 K. So the RMSE and the relative RMSE show completely contrary results. Probably because the differences in the RMSE are not as large as the temperature differences, which leads to this turn when I calculate the relative RMSE. So in fact, it would be best, if both values together are taken into account.

A feature appearing in several modeled profiles, which is also visible in Figs. 2.10b

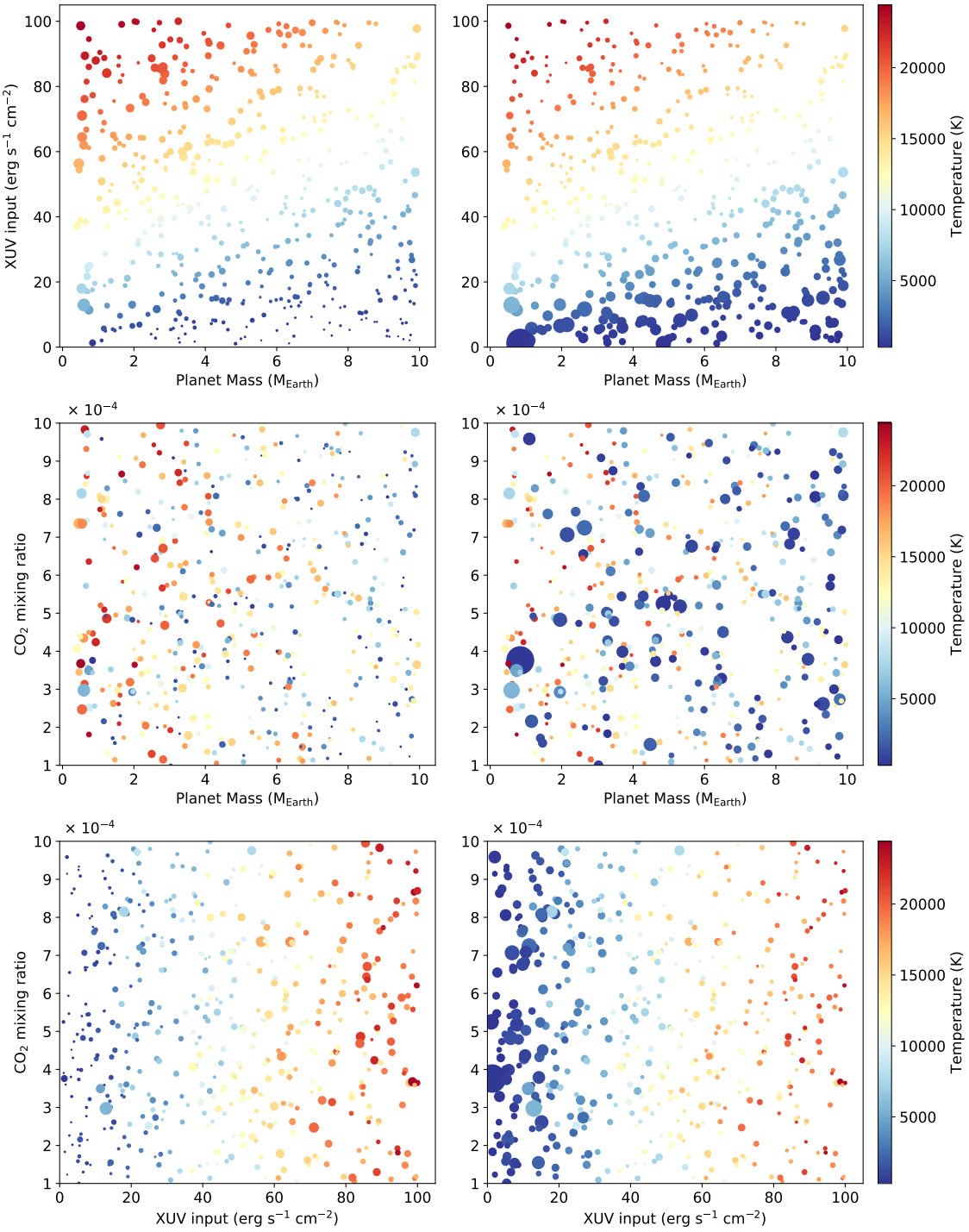

Figure 2.11: *Left column:* RMSE of the NN output compared to the reference profiles. *Right column:* Same as left column but divided by the temperature at the top of the reference profile.

and 2.10c are many small wiggles. They appear mostly at the top of the profiles, where the atmosphere is already in an isotherm regime but sometimes also at the bottom of the domain. These wiggles appear in profiles throughout the whole data grid, so they do not seem to be a feature of specific combinations of the input parameters but may simply be the result of too little training data.

Up to now, I have shown that my NN is able to reproduce the temperature profiles calculated with the simplified Kompot Code pretty good. The average RMSE is less than 15 K, which is very small concerning the fact that I use a very large range of possible input values for three different parameters and that the resulting temperature profiles cover a range between approximately 300 K up to almost 25,000 K. Yet, I still have to show one final property of my NN, which is in general one of the big advantages of a neural network: They generate their output a lot faster than any physical model does. To show this, I measured the time the simplified Kompot Code needs to calculate 512 temperature profiles with arbitrary values of the same input parameters as before. Afterwards, I measure the time the NN needs to produce the same profiles. The result is shown in Fig. 2.12. The blue histogram shows the time the simplified Kompot Code needs to calculate each profile, while the dashed red line shows how long my NN needs in total to calculate all 512 profiles. In other words, the simplified code needs almost 7 hours for 512 temperature profiles, whereas my NN can calculate them in less than 17 seconds. This means my model is more than 1400 times faster while keeping the accuracy at a quite high level.

Too small range of CO_2 mixing ratio

Throughout this section, I only considered CO_2 abundances between 1×10^{-4} and 1×10^{-3} and calculated the test and training profiles only for this range of input values. However, as I already showed in various diagrams, the resulting temperature profiles were mostly dependent on the size of the planet and the stellar radiation input. The exact value of the third input variable, the CO_2 mixing ratio, does not really make a difference. For example, the temperature profile of a planet with a CO_2 mixing ratio of 1×10^{-4} shows deviations of less than 2 K from the temperature profile of the same planet with the same radiation input but a CO_2 abundance of 1×10^{-3}. To emphasize this, I show two temperature profiles I calculated with the simplified Kompot Code in Fig. 2.13. I chose these two profiles because they have very similar planet masses and radiation inputs from the star but rather different CO_2 mixing ratios. Still the temperature profiles show next to no differences. Though the orange profile shows slightly smaller temperatures, the reason is rather the smaller XUV input than the higher CO_2 abundance in this simulation.

In fact, I should have chosen the range of the CO_2 abundances a lot bigger than just one order of magnitude. This range should have covered several orders of magnitude so that the influence can be seen properly.

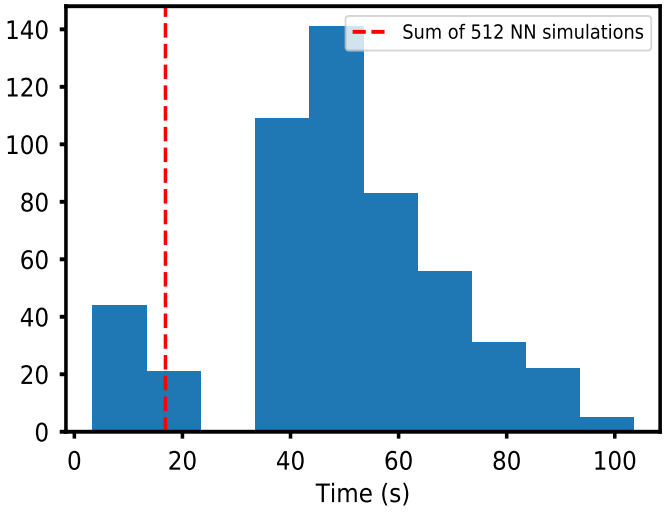

Figure 2.12: Histogram of the time the simplified Kompot Code needs to calculate one vertical temperature structure. In total 512 simulations are considered. The dashed line shows the overall time my NN needs to calculate all 512 profiles.

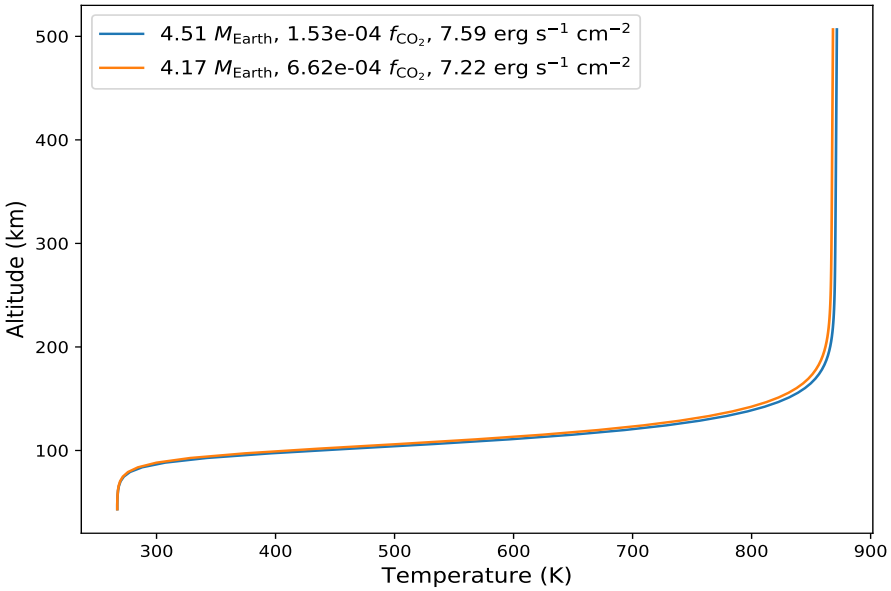

Figure 2.13: Two temperature profiles from the test data set. They have very similar masses and stellar XUV inputs but different CO_2 abundances. Still there are almost no differences in the resulting profiles.

3 Historical profiles for the early Earth

As I showed in the previous chapter, machine learning regression methods are very usable to model atmospheric temperature profiles of terrestrial planets around Sun-like stars although they are only given a few specific input quantities. In this chapter, I want to show that my NN can perform similarly good on an even more realistic data set, which is created using a model with much more physics in it than before. Moreover, this time the range of input CO_2 mixing ratios is much larger. So, I want to test the performance of the NN on a completely different and previously unknown data set.

Johnstone et al. (2021) used the full version of The Kompot Code to model Earth's mesosphere and thermosphere for different solar XUV fluxes and CO_2 abundances in the Earth's atmosphere during the Archean, a geologic eon of Earth's history spanning from approximately 4.0 to 2.5 Gyr ago. A basic assumption in their model was that the lower atmosphere was composed entirely of CO_2 and N_2, though other species could be created in their models by photodissociation and photoionization. They then derived historical thresholds for those two quantities given the constraints that Earth was neither completely frozen nor did it lose its entire atmosphere via escape to space. The authors made the resulting temperature profiles available for me to train and test a model using the setup of model 3 from Chap. 2.3.1. Using these temperature profiles and the hyper-parameters of the NN that I constrained in the previous chapter, I train a new neural network to predict the temperature profiles for the early Earth just from the input solar XUV flux and the atmospheric CO_2 mixing ratio. If my model is again capable of reproducing these temperature profiles properly, I can be confident about its performance in other similar applications. Since the full simulations with all of the included physical mechanisms took typically a few days each to calculate, the main advantage of using NNs is again the saving of time. After a sufficiently large set of models that covers the desired parameter space is calculated, NNs can be used to calculate arbitrarily large numbers of models in a negligible amount of time. Still, I want to keep the accuracy and reliability as high as possible.

3.1 Data set

For this chapter, I use the grid of models calculated by Johnstone et al. (2021), which consists of 86 cases that differ in CO_2 mixing ratio and solar input XUV spectrum. The CO_2 mixing ratio varies between 0.01% and 99% of the total atmospheric composition, representing the ability of the upper atmosphere to cool itself. The XUV fluxes vary between about 2–15 erg s^{-1} cm^{-2}. Each atmospheric model consists of vertical profiles for temperature, density, and chemical composition. Johnstone et al. (2021) used the full XUV spectrum as model input and expressed it in terms of time in the past from today in

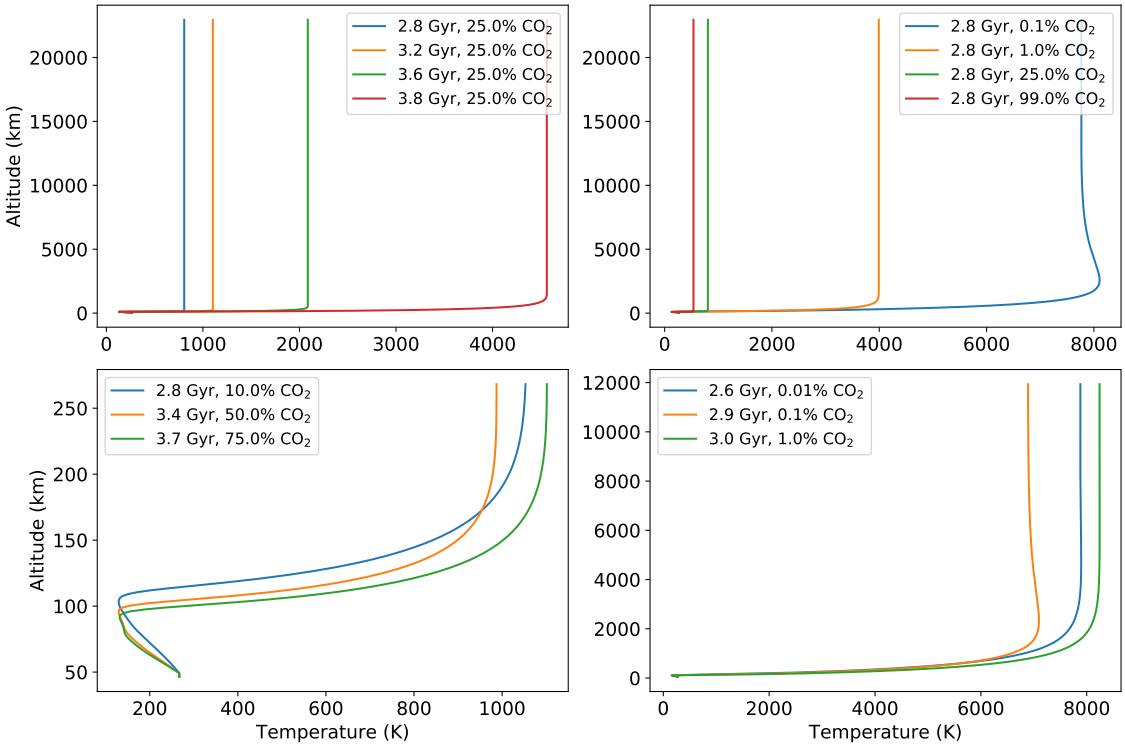

Figure 3.1: *Upper left:* Four temperature profiles resulting from simulations with the same atmospheric CO_2 mixing ratio of 25% and different XUV flux inputs. *Upper right:* Four vertical temperature structures resulting from simulations with the same XUV radiation input but different CO_2 abundances. *Lower left:* Three simulations, which lead to very similar temperature profiles, although the input parameters have quite different values. *Lower right:* Three simulations that lead to very high exobase temperatures due to the rather small CO_2 abundances.

Gyr, due to certain assumptions made about the solar radiation profile and its evolution over time. The XUV input decreases with time, which means that the XUV flux was higher in previous times of the Sun's evolution. One example for such a transformation between the age of a star and its radiation output can be found in Table 5 of Ribas et al. (2005). Johnstone et al. (2021) considered the first two bins of this table, i.e. a wavelength range between 1–100 nm. Note that Ribas et al. (2005) defined the timescale to be forwards from the beginning of the Solar System, while Johnstone et al. (2021) defined it to be backwards from today.

Fig. 3.1 shows several different temperature structures for different combinations of time in the past and atmospheric CO_2 mixing ratio. The upper left diagram shows four temperature profiles of simulations with different stellar XUV input but the same CO_2

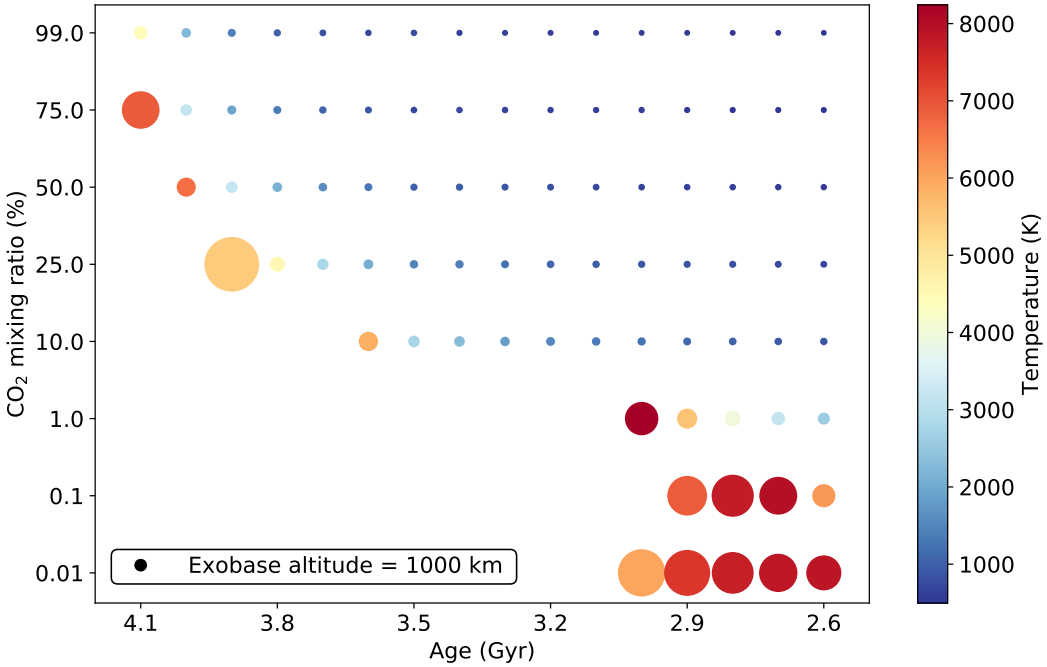

Figure 3.2: Height of the exobase for each simulation shown as marker size. The black dot in the lower left corner represents an exobase altitude of 1000 km. The exobase altitudes range from just above 140 km to more than 22,800 km. The marker color represents the temperature at the top of the simulation domain.

mixing ratio. It can be seen that during earlier states of the Sun's evolution the planet's atmosphere was much warmer if a constant CO_2 abundance is assumed. In the upper right panel I show the influence of the atmospheric CO_2 mixing ratio on the temperature profile. Higher amounts of CO_2 in the atmosphere lead to much lower temperatures given the same stellar insolation.

Similarly to what I mentioned in the previous chapter, a high XUV input together with a small CO_2 abundance leads to higher temperatures within the whole atmosphere and especially at the exobase because higher CO_2 mixing ratios would cool the upper atmosphere very effectively. Higher temperatures throughout the atmosphere also lead to more expanded envelopes and thus higher exobase altitudes (Johnstone et al., 2021). The lower right panel of Fig. 3.1 shows this correlation, since all three profiles result from simulations with very low CO_2 ratios. In fact even much higher exobase temperatures would be possible if early stages in the Sun's evolution were combined with very small CO_2 ratios. However, such profiles do not exist in the data set because the atmosphere would be removed under such circumstances within a rather short time. Therefore, these cases were not considered by Johnstone et al. (2021). The lower left panel shows examples of how different combinations of parameter pairs can lead to very similar temperature profiles. Although the blue and green curves represent simulations with much higher CO_2

abundances, 75% and 50% respectively, the exobase temperature is about the same as for the simulation with only 10% CO_2 (orange profile) because the atmosphere is less heated in this case. All the panels in Fig. 3.1 also show that the basic shape of all profiles is more or less the same and that this shape is basically the same as in the previous chapter. However, it is also evident that some features in the temperature profile can emerge that were not visible in the previous chapter. For example the temperature profiles in the lower left diagram show some small bumps at an altitude of about 80 km and are not as smooth as the profiles I calculated in Chap. 2. This is because of the fact that the reference profiles were calculated using the full instead of the simplified Kompot Code this time.

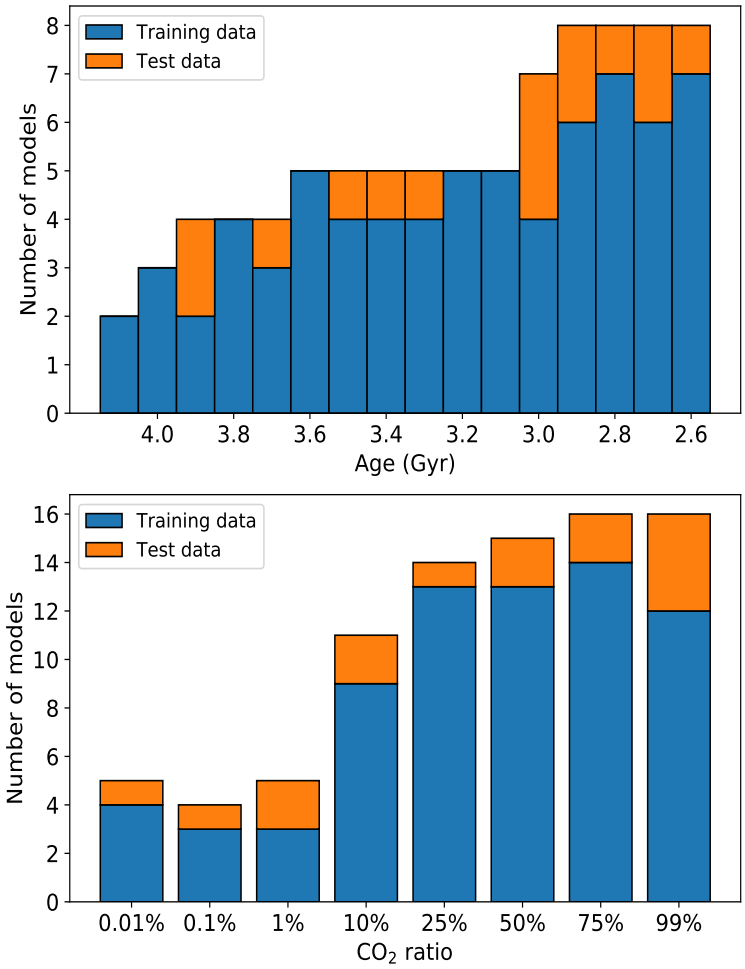

Figure 3.3: Value ranges for both input quantities and how they were split up into training and test data. The y-axis shows the number of simulations that belong to each bin.

It is important to note the ranges of the y-axis in all the panels of Fig. 3.1. The two diagrams in the top row extend over the maximal altitude range any of the profiles in the data set covers. The lower left one, which shows simulations with cooler atmospheres, extends to less than 300 km, while the simulations in the lower right one cover altitudes up to 12,000 km. Fig. 3.2 confirms the already mentioned correlation between exobase temperature and altitude since larger points (representing higher exobase altitudes) are always colored redder, which indicates higher temperatures at the top of the simulation domain.

The provided profiles span a time range corresponding approximately to the whole Archean as mentioned before, exactly a time range between 4.1 Gyr and 2.6 Gyr in the past. Fig. 3.3 shows a bar chart of all available profiles, the values of their input quantities and if they belong to the training or test data set. Since I need enough data for both calibration and validation of my NN, I decide to use 71 profiles for training and the remaining 15 for testing. I did the division which profile belongs to which subset randomly. Thus, not every age bin is represented in the test data set but I can still do the verification of the model performance sufficiently enough.

One drawback of the data is that the upper boundary of the exosphere is not fixed to 500 km as before because of the previously mentioned highly variable exobase altitude (see again Figs. 3.1 and 3.2). But in order to train the model properly, all the input data has to be on the same grid. Therefore, I expand the domain of every simulation up to the maximum exobase altitude appearing in any of the simulations. Above the exobase of each simulation I assume an isotherm atmosphere and add equally spaced grid points with constant temperature values.

So in fact I have a data set consisting of 86 vertical temperature structures each one ranging from 50 km above the planet's surface up to an altitude of almost 23,000 km. 71 of them belong to the training and the other 15 to the test data set. So, this time I have much less profiles available to train and test my NN than before but according to the very good results in the previous chapter, I still expect a rather good performance now.

3.2 Neural Network

To test the performance of the NN setup derived in Chap. 2, I use a model consisting of four hidden layers with 250 nodes each and train it for a maximum of 25,000 epochs. Again I save the best model, i.e. the one with the smallest MSE, rather than the one after the last training epoch. The minimum MSE is about 1.9×10^{-5} K^2 after 22,956 training epochs, which is approximately 10 times more than in the training process in Chap. 2 (see Fig. 2.8). However, the number of training epochs is almost the same as before although the number of training epochs was allowed to vary in a quite large range. The reason for the larger MSE is most probable the much smaller amount of available data together with the more complex shape of the profiles. After the calibration process, I validate the model performance using the 15 profiles in the test data set.

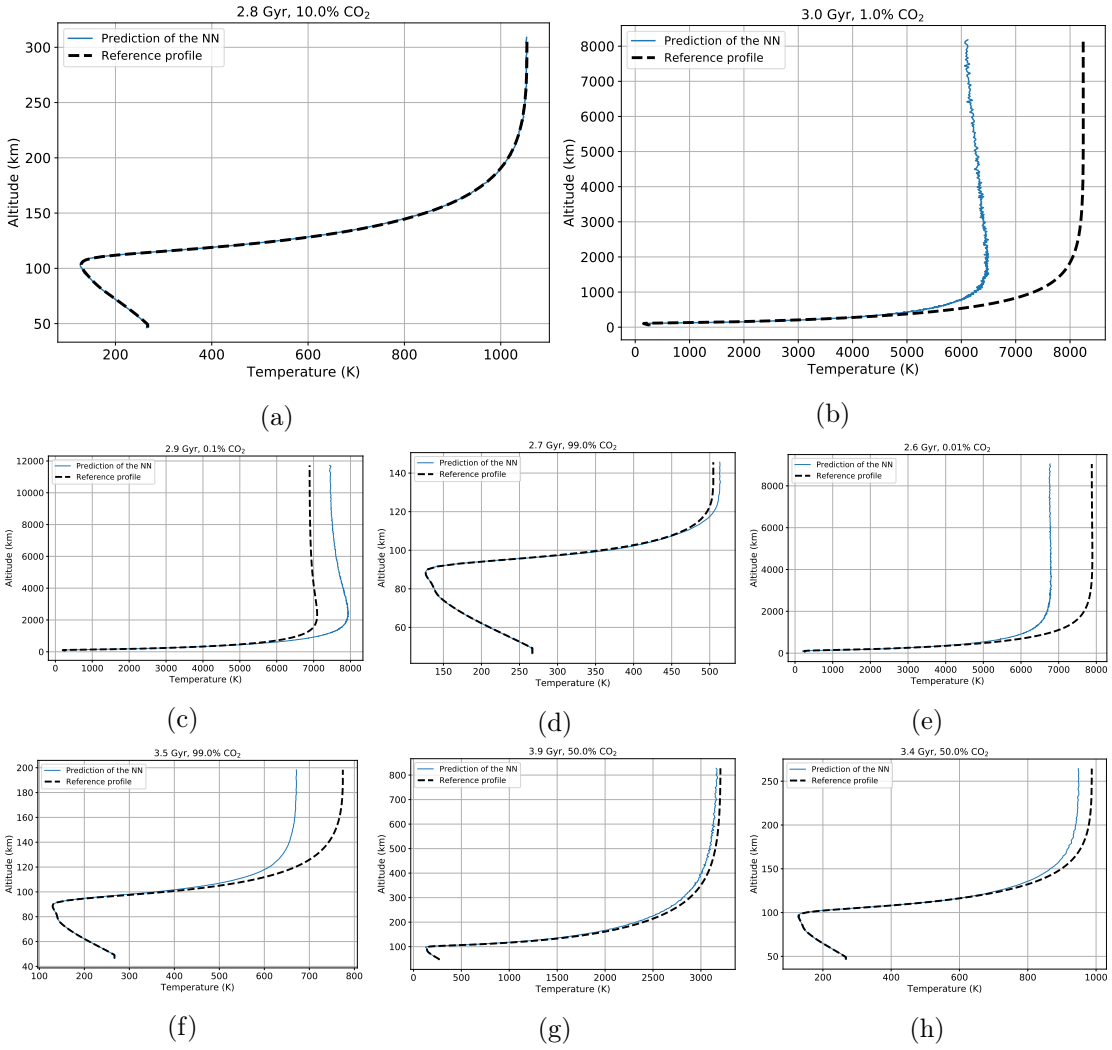

Figure 3.4: The best (a) and worst (b) performance of my NN compared to their respective reference profile together with six further diagrams comparing the NN output to the reference profiles.

3.3 Results

Fig. 3.4 shows several examples of the model output compared to the reference profiles (dashed lines). The top row shows the best and worst performance of my NN on the test data set. In the middle and bottom row I show six more diagrams, which show that a broad range of fit qualities is possible. It can be seen that for the sake of representation I cut off the profiles in the region where I assume the exobase before showing them. Otherwise no structure at all would be visible in most of the cases. I estimated the exobase altitude to be where the reference profile becomes isothermal. As before, the NN is often able to perfectly reproduce the reference profile (see Fig. 3.4a). However, the upper right panel (Fig. 3.4b) shows that also deviations between the exobase temperatures of up to 28% are possible, which could be significant in certain cases if the NN is used to predict the temperature profiles.

Although several panels in Fig. 3.4 show a big deviation between both profiles, the mean relative error of all test profiles is only about 5%. Fig. 3.5 shows the RMSE for every simulation in the test data set. As in the previous chapter, the area of each point shows the error size and its color represents the temperature at the exobase. As in Fig. 2.11 the left panel of Fig. 3.5 shows the absolute RMSE and the right one the relative RMSE, i.e. the absolute RMSE divided by the temperature at the exobase of each simulation. The biggest errors occur for simulations with high exobase temperatures. The mean relative errors of simulations with CO_2 ratios $\leqslant 1\%$ range between 6.5% and almost 18% while only one of the others exceeds a mean relative error of 5.4%. Without these four profiles the mean relative error reduces to only about 3%. The reason for such high errors is, at least partially, again based on the high exobase temperature found in profiles with such small CO_2 abundances. It can be seen in the right panel of Fig. 3.5 that 3 of the four biggest relative RMSEs occur in simulations with CO_2 ratios $\leqslant 1\%$.

Although the errors can look large in a few cases, most of the relative RMSEs are only a few percent of the respective exobase temperature, which is insignificant and much less than other uncertainties present in the models. The maximum occurs for the simulation with a CO_2 abundance of 1% at 3.0 Gyr ($\approx 15.6\%$), which shows an exobase temperature of more than 8200 K. The simulation with the smallest relative RMSE ($\approx 0.2\%$) is the one with 10% CO_2, 2.8 Gyr in the past and an exobase temperature of just above 1000 K. This behaviour is quite contrary to the one I obtained in the previous section. There, simulations with high exobase temperatures also had higher absolute RMSEs but smaller relative RMSEs. This time, the high temperature simulations have both high absolute and high relative RMSE values. What Fig. 3.5 also shows is that the region with the second highest errors (both absolute and relative RMSE) is represented by profiles corresponding to earlier evolution stages, i.e. 3.5–3.9 Gyr in the past. Yet they are much smaller than for profiles with $\leqslant 1\%$ CO_2 abundance. Another factor contributing to those large errors in both groups is probably the fact that there are only a few training profiles available in the corresponding value ranges. For CO_2 mixing ratios of 10% and more I have at least 11 profiles per bin available but below this threshold there is only a total of 14 profiles in 4 bins of which only 10 are in the training data set. Similarly, there are only 2 to 4 training profiles in most of the age bins from 3.5–4.1 Gyr but up to 7 in each of the other

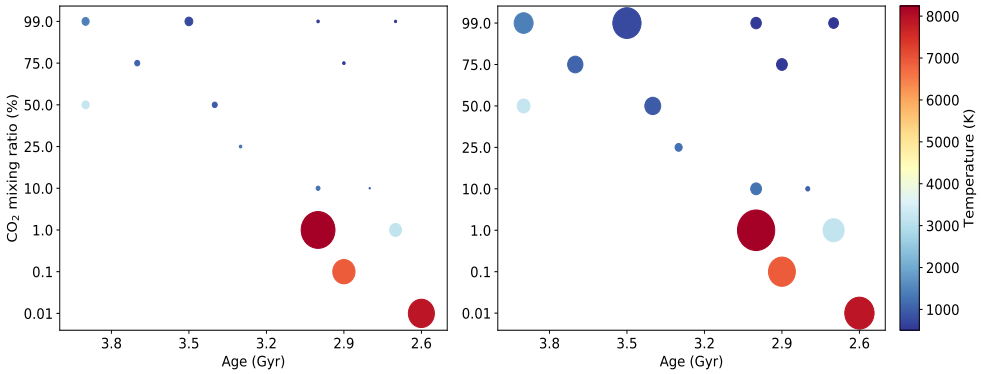

Figure 3.5: *Left panel:* Absolute RMSE of the 15 test profiles of the data set with historical Earth setups as size of the markers. *Right panel:* Relative RMSE, i.e. absolute RMSE divided by the exobase temperature. The exobase temperature is represented by the marker color in both panels.

age bins (see Figs. 3.2 and 3.3). On the other hand, the smallest absolute and relative RMSEs are located in the upper right corner of Fig. 3.5, since I have enough training data available in the corresponding value ranges and the exobase temperatures are also not that high. There was no such behaviour visible in Chap. 2 because I had enough training data available over the whole range of possible input values.

Another factor contributing to higher errors in this section is that the training and test data is much more complex, which can again be seen in Fig. 3.4. Not only that there are more small features like bumps in the temperature profiles, they also extend to much higher altitudes than before. Together with the smaller amount of profiles, this surely is a reason for the higher RMSEs.

In summary, this chapter showed that my NN is able to reproduce the vertical temperature profiles produced by a more realistic physical model, and is able to do this with a modest number of training profiles. A more detailed look at how many profiles are needed to get various levels of accuracy would be a useful point for future studies.

4 Evolution of thermospheric temperature for different stellar masses and initial rotation rates

In the previous two chapters, I showed that neural networks are capable of calculating temperature structures of upper atmospheres even for a quite wide range of input parameters. One requirement is a sufficient amount of training data. Since this requirement is fulfilled for the model I trained in Chap. 2, I am now going to show one possible application of this NN. I want to calculate temperature profiles of a planet similar to modern Earth for different evolutionary steps of its parent star. For my NN, I need three input parameters: these are the mass of the planet, the CO_2 mixing ratio in the atmosphere and the stellar input XUV flux. For the first two parameters, I use the values for modern Earth, i.e. $M_{\rm pl} = 1.0$ M$_\oplus$ and $f_{\rm CO_2} = 4 \times 10^{-4}$, and to get the stellar XUV input flux, I use the stellar evolution model MORS.

4.1 Model for Rotation of Stars (MORS)

MORS is a physical model by Johnstone et al. (2020) calculating the full stellar rotation and XUV evolution of stars with masses in a range between 0.1 and 1.2 M$_\odot$, and ages from 1 Myr until the end of the main-sequence. The model calculates the evolution of a star's rotation rate taking to account changes in its internal structure and angular momentum losses. For the former, the stellar evolution models of Spada et al. (2013) are used. For the latter, the main angular momentum loss process is from magnetized stellar winds, with a simple parameterization of angular momentum exchanges being used in the first few Myr. Additionally, the redistribution of angular momentum within the star is considered. The rotation model is constrained by a large number of stellar rotation measurements in 12 young clusters. The XUV emission is calculated from the rotation tracks using empirical rotation–X-ray and X-ray–EUV relations. The model is able to calculate evolutionary tracks for stellar rotation as well as many other parameters given only its mass and initial (1 Myr) rotation rate because these are the two main parameters that determine its XUV evolution (Johnstone et al., 2020). The parameters that are important for me are the X-ray, extreme UV, and Lyman-α emission of the star in its habitable zone (HZ). Here the X-ray and extreme UV bands cover a wavelength range from 0.517–92 nm and the Ly-α emission line is located at 121.5 nm. Taken together, this fits the wavelength range between 0.1–120 nm, in which I considered the input XUV flux, very well. The orbital distances of the HZ at all ages are calculated as functions of stellar mass and age using the formulae of Kopparapu et al. (2013) and the stellar models of

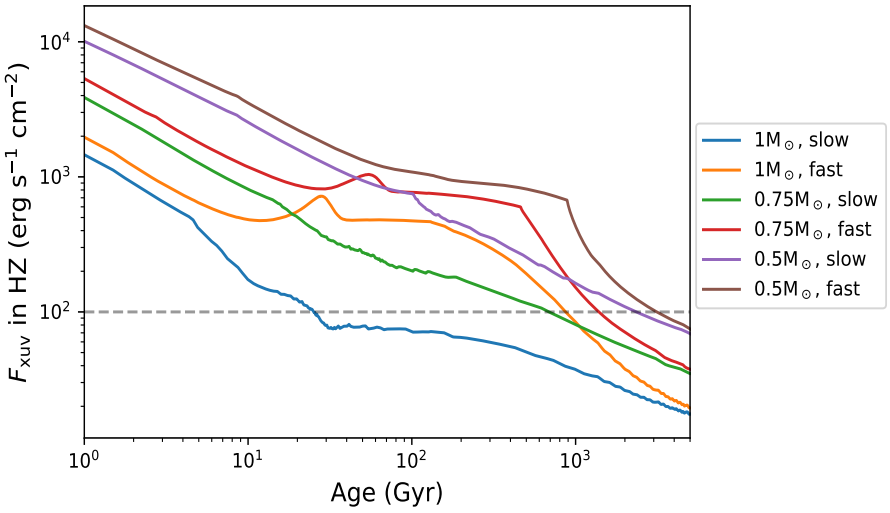

Figure 4.1: Temporal evolution of $F_{\mathrm{xuv,HZ}}$ for six stellar models with different stellar masses and initial (1 Myr) rotation rates. The dashed line shows the upper boundary of input values for the NN I trained in Chap. 2.

Spada et al. (2013) because the bolometric luminosity is, together with the star's effective temperature, the main factor determining these borders (Kasting et al., 1993). However, I have to mention that I do not take into account the stellar variability in my work. For example, Stern et al. (1995) found from comparisons of *Einstein* and ROSAT data that the X-Ray luminosity of main-sequence Hyades K and M stars varies up to a factor of 2. Schmitt et al. (1995) confirmed this result for the solar neighborhood. The evolutionary tracks calculated with MORS just show the average luminosity of a star at a given age, the true value can vary by quite a lot, mostly because of flares or cycles.

It is also important to note that the MORS model overestimates the modern Sun's XUV emission. Partly this is likely because the Sun appears to be less active than stars with similar masses, ages, and rotation rates (Reinhold et al., 2020), and partly this could be due to uncertainties in the slope of the relation between rotation and X-ray emission for unsaturated stars (e.g. Reiners et al., 2014).

Using MORS, I simulate six different stars which I assume then to be the host stars of the planet I described previously. I use three different stellar masses, 0.5 $M_\odot$, 0.75 $M_\odot$ and 1.0 $M_\odot$ and two different rotation rates each, which are simply called slow and fast rotation. They are defined as the 5$^{\mathrm{th}}$ and 95$^{\mathrm{th}}$ percentiles of the rotation distribution given by several observed clusters (Irwin et al., 2007, 2009; Meibom et al., 2009; Hartman et al., 2010; Rebull et al., 2016) with ages of approximately 150 Myr. The *slow* rotation rate of the star at 1 Myr is approximately 1.52 times the rotation rate of the modern Sun, which was set to $\Omega_\odot = 2.67 \times 10^{-6}$ rad s^{-1} by the authors of the code. The *fast* rotation rate results in ca. 24.98 $\Omega_\odot$.

For each of these six stars, I calculate the rotational evolution and the resulting total

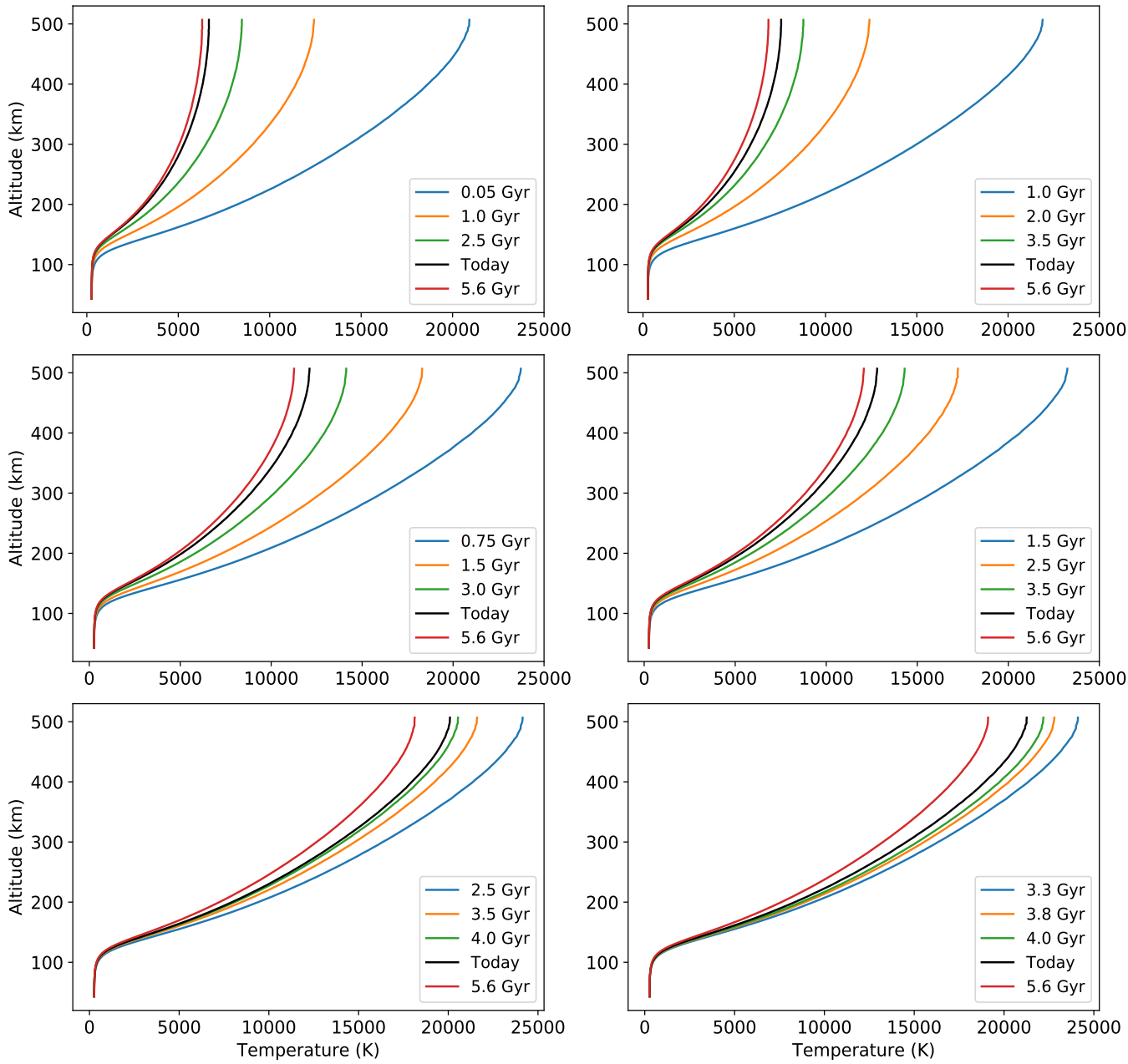

Figure 4.2: Temperature profiles of a planet with 1 Earth mass and a CO_2 abundance of 4 $\times 10^{-4}$ around six different stars at 5 different times during the star's evolution. The star's mass is 1 $M_\odot$, 0.75 $M_\odot$ and 0.5 $M_\odot$ in the first, second and third row, respectively. The left column shows initially (1 Myr) slow and the right column initially fast rotating stars.

X-ray, EUV, and Ly-alpha emission in their respective HZs. I call this quantity $F_{\mathrm{xuv,HZ}}$ hereafter and its evolution is shown in Fig. 4.1 for the six stars. Since I trained my NN only with stellar fluxes between 1 and 100 erg s^{-1} cm^{-2}, I can only use input values of $F_{\mathrm{xuv,HZ}}$ within this specific value range. The upper boundary of possible input values is shown as dashed line in Fig. 4.1. Because of this restriction, I can consider every star only after a certain age, and this threshold age is dependent on its mass and initial rotation rate and varies a lot between the individual stars. For example, an initially slow rotating star with a mass of 1 $M_\odot$ crosses this line already after about 25 Myr, while an initially fast rotating star with a mass of 0.5 $M_\odot$ crosses it only after 3 Gyr. One reason for this behaviour is that lower mass stars evolve slower than those with higher masses, both in internal structure and in rotation, and consequently remain active longer, and the other reason is that those stars that are initially fast rotators remain active longer and therefore also emit more XUV radiation than initially slow rotating stars (Johnstone et al., 2020). This is also visible in the tracks shown in Fig. 4.1. All the initially slow rotating stars show a persistent decay of the emitted XUV radiation. Those that rotate faster when they are born also show a decay, but afterwards even a short epoch of rising XUV emission (at least the more massive ones), a small plateau and then a decay again. Although higher mass stars are more XUV luminous than lower mass stars, the orbital distances of their habitable zones are also larger leading to planets orbiting low mass M dwarfs receiving X-ray fluxes that are two orders of magnitude higher than those received by planets orbiting G dwarfs at 5 Gyr (Johnstone et al., 2020).

4.2 Results

4.2.1 Evolution of an Earth-like atmosphere on an Earth-mass planet

In this section, I consider the evolution of the atmospheric temperature profile for an Earth-mass planet with a CO_2 mixing ratio of 4×10^{-4}, which is similar to that of the modern Earth, and assume that the planet is in the center of the habitable zone of its host star. I study this case for all six stellar evolution scenarios discussed above. To do this, I take the XUV flux of the star in its HZ $F_{\mathrm{xuv,HZ}}$ at five different points in its evolution and use it as input for my NN trained in Chap. 2 together with the planet's size and the atmosphere's CO_2 abundance. Three of these ages are from the past, one is at an age of 4.6 Gyr, referred to as *Today*, and one is approximately 1 Gyr in the future. In Fig. 4.2 I show the results for the six stars I described previously. The first, second and third row show stars with a mass of 1 $M_\odot$, 0.75 $M_\odot$ and 0.5 $M_\odot$, respectively. The left column shows initially (1 Myr) slow and the right one initially fast rotating stars. It can be seen that a lower mass host star leads to higher temperatures throughout the atmosphere of an orbiting planet. Moreover, higher temperatures are also reached, especially at the exobase, if the star is an initially fast rotator. Note that the individual ages for which I show the temperature structures are different every time since each star's XUV emission in its habitable zone decays below 100 erg s^{-1} cm^{-2} at a different age (see Fig. 4.1).

The upper atmospheric temperature profiles of a planet around a slow rotating solar mass star at five different ages are shown in the upper left diagram in Fig. 4.2. After the

results in Fig. 4.1 it is not surprising that the planet's atmosphere reaches the highest temperatures during early evolutionary stages of the star with an exobase temperature of more than 20,000 K. However, after 2.5 Gyr the temperatures are already much smaller with an exobase temperature of almost 8500 K, and as the star evolves the temperature continues to decrease. Even at an age of 5.6 Gyr, the stellar $F_{\mathrm{xuv,HZ}}$ was more then 16 erg s^{-1} cm^{-2}, which is approximately 4 times the amount of radiation I assumed for the Earth case at the beginning of this work and the exobase temperature of the planet is still as high as 6300 K.

The right diagram in the second row of Fig. 4.2 shows the evolution of the upper atmospheric temperature profile of the same planet around an initially fast rotating star with $M_* = 0.75$ $\mathrm{M}_\odot$. Given how the XUV emission of the stars evolves differently for different masses and initial rotation rates, it is not surprising that the temperature profiles around this star with a lower mass but a faster rotation rate show much higher temperatures. This becomes evident if one compares the planetary temperature profiles at ages of 2.5, 4.6 and 5.6 Gyr of the upper left and the middle right panel of Fig. 4.2. The atmospheric temperatures at high altitudes for planets orbiting lower mass stars are approximately twice as high as around the solar mass star. Concerning a host star with a mass of 0.5 $\mathrm{M}_\odot$, one can see that the exobase temperature is even in the future very high, with values up to 19,000 K.

As we have already seen, the planet's exobase temperature changes a lot during the evolution of its parent star. In Fig. 4.3, I show the temporal evolution of the temperature at the top of the atmosphere of three test planets with different masses located inside the HZ of the six stars I modeled. The upper, middle and lower panel show a planet with a mass of 5.0 $\mathrm{M}_\oplus$, 1.0 $\mathrm{M}_\oplus$ and 0.5 $\mathrm{M}_\oplus$, respectively. Each of them has an atmospheric CO_2 abundance of 4×10^{-4}, which is very similar to today's Earth. As before, the evolutionary periods that I consider start when the stellar XUV emission drops below 100 erg s^{-1} cm^{-2}. I set the upper boundary for the age of the star to approximately 1 Gyr in the future, according to the timescale I used in the previous plots. As shown in the XUV emission curves in Fig. 4.1, the exobase temperature decays faster around planets with higher masses. The temporal evolution curves of the exobase temperature demonstrate that the lower the mass of the star, the higher the amount of XUV radiation received by HZ planets and thus also the higher the exobase temperature. In fact, the temperature at the exobase of a planet around a star with $M_* = 0.5$ $\mathrm{M}_\odot$ at an age of 4.6 Gyr is approximately three times as high as the exobase temperature of the same planet around a solar mass star of the same age. The difference is even larger for a higher mass planet. As I already showed in the previous chapters, in general the temperature at the exobase of lower mass planets reaches higher values than the exobase of a more massive planet under the same circumstances. However, there is not much difference between the exobase temperatures of the Earth mass planet and the one with a mass of 0.5 $\mathrm{M}_\oplus$ (middle and lower panel of Fig. 4.3, respectively). It is also evident that the upper atmosphere of a planet is slightly hotter if its parent star is a rapid rotator rather than a slow one. I have to note that the small wiggles in the profiles of the solar mass stars do not come from my NN. They can already be seen in the radiation profiles I get from MORS, so maybe they come originally from the stellar models of Spada et al. (2013).

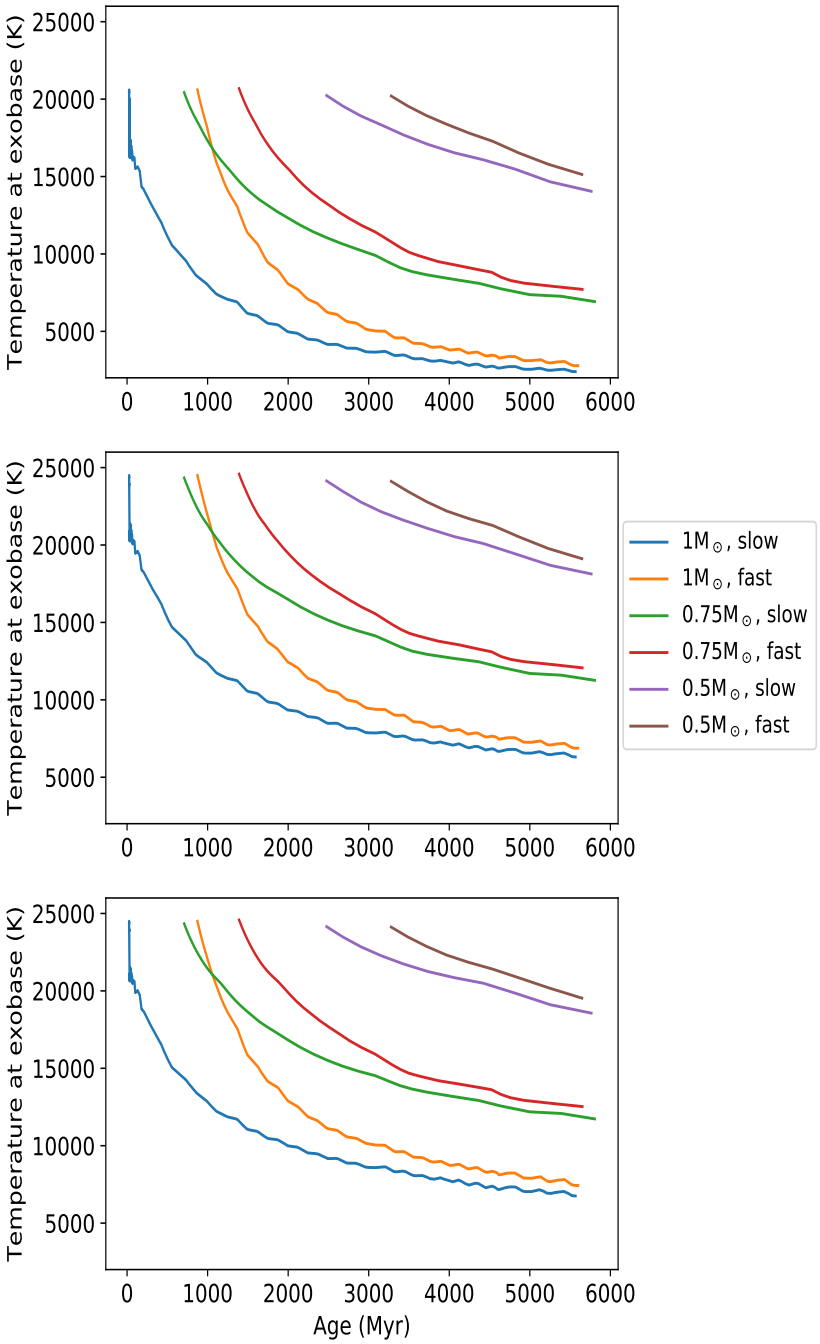

Figure 4.3: Temporal evolution of the temperature at the exobase of a planet with $M_{\mathrm{pl}} =$ 5.0 $M_{\oplus}$, 1.0 $M_{\oplus}$, and 0.5 $M_{\oplus}$ (upper, middle and lower panel, respectively) and a CO_2 abundance of 4 $\times 10^{-4}$ in the HZ of each star I modeled.

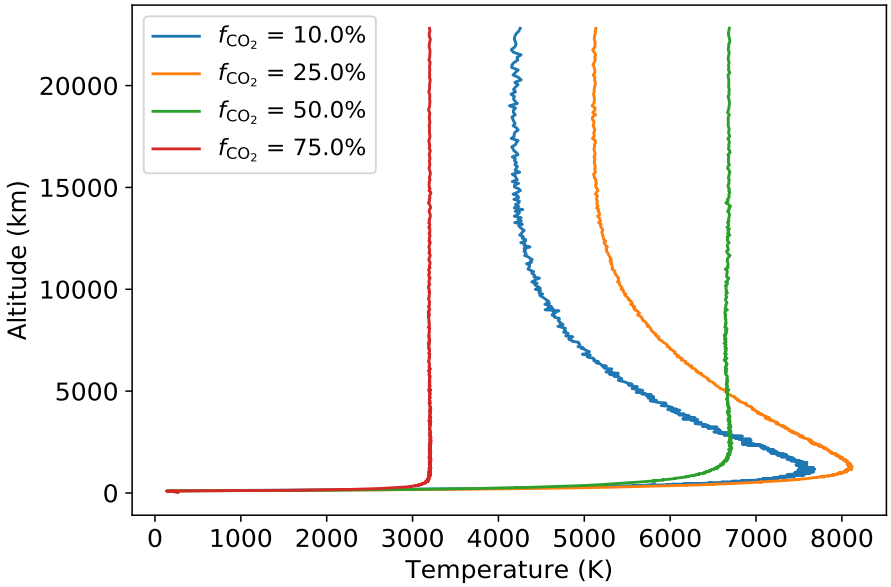

Figure 4.4: The upper atmospheric temperature profiles of an Earth mass planet within the HZ of an initially slow rotating solar mass star, receiving an XUV radiation flux of approximately 16.3 erg s^{-1} cm^{-2} and assuming four different CO_2 mixing ratios in the atmosphere of this planet.

4.2.2 Higher CO_2 abundances in the atmosphere of an Earth-mass planet

As I already mentioned at the end of Chap. 2, the range of input CO_2 abundances I defined for my NN was too small to show the effect of CO_2 on the vertical structure of the atmospheric temperature. But still I want to investigate its influence on the upper atmospheric temperature profiles. Therefore, I use the NN trained in Chap. 3 to calculate another set of temperature structures but with slightly different input variables than in the previous section. This time, the planet's mass is fixed to 1 $M_\oplus$ due to the data set I used to train the model. In this model also the possible range of XUV radiation input values was much tighter than before. I mentioned in Chap. 3 that Johnstone et al. (2021) only used XUV input spectra between 2–15 erg s^{-1} cm^{-2}. Reconsidering the fluxes inside the HZ of each modeled star in Fig. 4.1 it can be seen that none of them decays below this upper border of 15 erg s^{-1} cm^{-2} until an age of 5 Gyr. However, if I extend the age range up to 10 Gyr the two simulations of the solar mass stars, which showed the smallest XUV fluxes, come at least very close to this threshold. In fact, the smallest value of $F_{\mathrm{xuv,HZ}}$ I obtained in any of the six simulations is approximately 16.3 erg s^{-1} cm^{-2} when considering an initially slow rotating solar mass star at an age of about 7.3 Gyr. This value is close enough to the threshold to be still usable in my NN. To use it as input, I have to transform it into an age bin using the transformation relation from Ribas et al. (2005) I already mentioned. Finally, I can choose almost arbitrary values for the other

input parameter of my model, which is the CO_2 mixing ratio. Although the training data only used discrete CO_2 abundance bins, it is no problem, if any other value is used as an input.

Fig. 4.4 shows the upper atmospheric temperature profiles of an Earth mass planet within the HZ of an initially slow rotating solar mass star, receiving an XUV radiation flux of approximately 16.3 erg s^{-1} cm^{-2} and assuming four different CO_2 mixing ratios in the atmosphere of this planet. It is very interesting that the two simulations with the highest assumed CO_2 mixing ratios show the highest and lowest exobase temperatures and the two with smaller CO_2 abundances can be found in between. Moreover, the shapes of these two profiles with a mixing ratio of 10% and 25% are very different than the others. They both show a temperature peak at an altitude of about 1500 km and decreasing temperatures towards higher altitudes. If the shape of the profiles with CO_2 abundances of 10% and 25% would be the same as for the other two simulations the exobase temperatures would be a lot higher. Maybe these lower CO_2 abundances even warm the lower atmospheric layers and only cool the upper ones, while high mixing ratios cool all layers similarly.

Another possibility is that my NN cannot handle these low CO_2 abundances together with a relatively high XUV input. Reconsidering Fig. 3.2, one can see that at ages where such high input fluxes are used, the available CO_2 mixing ratios in the data set are 50% or higher. Another hint for this problem can be seen in Fig. 4.4 where the profile of the simulation with $f_{CO_2} = 10\%$ shows way more wiggles than the others, representing possible uncertainties of the model. However, I also compared these profiles to some of the training data set with a very similar input and this showed that my NN delivers very good results. At least the profiles with CO_2 abundances of 25%, 50% and 75% are very reliable. And again, the NN saves a lot of time compared to one simulation of the full Kompot Code.

5 Conclusions

The aim of my work was to show the ability of modern machine learning regression methods to calculate vertical temperature profiles for upper atmospheres given only a few input parameters, and to demonstrate how such methods can be used in studies of atmospheric evolution. One main advantage of this method is the large amount of time which is saved when a NN is used compared to the hours or even days one full simulation needs to calculate such a profile. While NNs cannot substitute for detailed physical models, they can be trained on the results of such models, allowing arbitrarily large numbers of atmospheric profiles to be generated in negligible time with similar accuracies to the physical models.

The basis of my work is The Kompot Code, a first-principles physical model for planetary atmospheres. I used both the results of the full version of this code and a simplified and thus more efficient version in this project. With the latter, I created more than 1000 vertical temperature profiles for altitudes between 50 km and 500 km above the planets surface. To create them I defined a grid of simulations where I assigned random values between well-defined borders to three input parameters, namely the size of the planet (mass and radius), the CO_2 abundance in the atmosphere and the stellar XUV flux input. I fit to this set of models a grid of neural networks, varying the number of hidden layers, the number of neurons per hidden layer, and the number of steps in the training algorithm. Then I used the temperature profiles I calculated to train and test every NN in the grid in the same way to find out which setup of these hyper-parameters shows the best performance. I made the decision based on the mean squared error of both the training and the test process. The NN which delivered the best results consists of 4 hidden layers with 250 nodes per layer and is trained for 22,878 epochs. At the end of the training process the MSE of this model was $< 2 \times 10^{-6}$ K^2. The average RMSE over all test profiles was less than 15 K and although some profiles could not be reproduced very accurately most of them actually could. Although the largest root mean square errors occurred in simulations with very high temperatures at the exobase the RMSE normalized to this temperature is the smallest for this kind of simulations. In addition, the average simulation with my NN lasts less than a tenth of a second, while it can take up to several days to run one single simulation with the physical model. Over the whole grid, my NN showed very good results concerning accuracy, calculation time and reliability.

I also verified the good performance of my NN using another data set from Johnstone et al. (2021). This data consists of vertical temperature profiles calculated with the full Kompot Code assuming conditions under which the Earth evolved between 4.1 Gyr and 2.6 Gyr in the past. I used the previously described NN setup again, trained and tested it with this historical data to see if it can perform similarly well. Although the results were not as good as before (MSE of the training process $\approx 1.9 \times 10^{-5}$ K^2, RMSE of all

test profiles ≈ 203 K), I am still very satisfied because I only had 71 temperature profiles available to train the NN compared to over 500 I had before. Still, in the value ranges where I had a sufficient amount of training data the RMSE is only 26 K which is a very good result under these circumstances. So my NN also performed very well on this new data set.

To demonstrate the potential of these methods, I used the NN trained on the larger dataset from Chap. 2 to derive the evolution of the thermospheric temperature profile of an Earth-mass planet under different circumstances. For this purpose, I used the MORS model by Johnstone et al. (2020) to calculate stellar evolutionary tracks for 6 stars with different masses (0.5 $M_\odot$, 0.75 $M_\odot$ and 1.0 $M_\odot$) and initial rotation rates (*slow* corresponding to approximately 1.52 $\Omega_\odot$ and *fast* corresponding to about 24.98 $\Omega_\odot$). The quantity I look at is the XUV flux in the HZ of each star $F_{\mathrm{xuv,HZ}}$. Then I used the NN of Chap. 2 and calculated the temperature profiles of a planet very similar to today's Earth at five different ages during the evolution of each modeled star. The only changing input parameter is $F_{\mathrm{xuv,HZ}}$, which constantly changes during the star's evolution. I also considered the evolution of the exobase temperature of three planets with masses of 5.0 $M_\oplus$, 1.0 $M_\oplus$ and 0.5 $M_\oplus$ around these stars. I showed that the temperature at the top of the atmosphere of such a planet is more than 20,000 K if its host star is an initially fast rotating star with $M_* = 0.5\ M_\odot$ at an age of 4.6 Gyr compared to less than 7000 K if it orbits an initially slow rotating solar mass star of the same age. Moreover, the results showed that the temperature in the upper atmosphere of this planet changes through the evolution of its parent star by several 10^3 K.

In order to consider the effect of the amount of CO_2 in the planet's atmosphere too, I also used the NN from Chap. 3. Since the XUV radiation in the training data set only covered a very narrow range, I could only use the initially slow rotating solar mass star at an age of about 7.3 Gyr as host star for my hypothetical planet. Then I calculated the planet's upper atmospheric temperature profiles considering 4 different CO_2 abundances. These profiles were shaped rather differently for cases with small and high mixing ratios. Moreover, a higher CO_2 abundance does not automatically mean that the temperatures in the atmosphere have to be smaller. In fact, the models with $f_{CO_2} = 10\%$ and $f_{CO_2} = 25\%$ showed a temperature maximum at an altitude of approximately 1500 km and a decay above. This maximum could not be found in the other two simulations. A possible explanation could be that CO_2 does not cool the entire atmosphere but can also heat the lower layers and only cool the upper ones. Although I had not much training data available for this model, I am still very confident about the resulting temperature profiles.

In summary, in my work I showed that modern machine learning regression methods are a very reliable way to calculate vertical temperature profiles of upper atmospheres under a very broad range of input parameters. If the NN setup is chosen properly and enough training data is available, its performance is very accurate and most important it is also a lot faster than sophisticated hydrodynamic models are.

Since I used a much too small range of CO_2 input values in this work, it would be very interesting to investigate the effect of this parameter on the temperature profile in future studies. Future work may also cover the amount of training data that is needed for NNs in order to reach a certain accuracy for a given number of input parameters

since more input parameters lead to a more complex training process. In addition to this, also profiles of quantities other than the temperature could be fitted using modern machine learning regression methods. Examples may be the atmosphere's density or the abundances of main chemical species throughout the atmosphere.

Bibliography

Abadi, M., Agarwal, A., Barham, P., Brevdo, E., Chen, Z., Citro, C., Corrado, G. S., Davis, A., Dean, J., Devin, M., Ghemawat, S., Goodfellow, I., Harp, A., Irving, G., Isard, M., Jia, Y., Jozefowicz, R., Kaiser, L., Kudlur, M., Levenberg, J., Mané, D., Monga, R., Moore, S., Murray, D., Olah, C., Schuster, M., Shlens, J., Steiner, B., Sutskever, I., Talwar, K., Tucker, P., Vanhoucke, V., Vasudevan, V., Viégas, F., Vinyals, O., Warden, P., Wattenberg, M., Wicke, M., Yu, Y., and Zheng, X. (2015). TensorFlow: Large-Scale Machine Learning on Heterogeneous Systems. Software available from tensorflow.org.

Amerstorfer, U. V., Gröller, H., Lichtenegger, H., Lammer, H., Tian, F., Noack, L., Scherf, M., Johnstone, C. P., Tu, L., and Güdel, M. (2017). Escape and evolution of Mars's CO2 atmosphere: Influence of suprathermal atoms. *Journal of Geophysical Research: Planets*, 122(6):1321–1337.

Basilevsky, A. T. and Head, J. W. (2003). The surface of venus. *Reports on Progress in Physics*, 66(10):1699–1734.

Bottaci, L., Drew, P. J., Hartley, J. E., Hadfield, M. B., Farouk, R., Lee, P. W., Macintyre, I. M., Duthie, G. S., and Monson, J. R. (1997). Artificial neural networks applied to outcome prediction for colorectal cancer patients in separate institutions. *The Lancet*, 350:469–472.

Catling, D. and Zahnle, K. (2009). The Planetary Air Leak. *Scientific American*, 300:36–43.

Chabrier, G. and Baraffe, I. (2000). Theory of Low-Mass Stars and Substellar Objects. *Annual Review of Astronomy and Astrophysics*, 38:337–377.

Chollet, F. et al. (2015). Keras. `https://keras.io`.

de Wit, J., Wakeford, H. R., Lewis, N. K., Delrez, L., Gillon, M., Selsis, F., Leconte, J., Demory, B.-O., Bolmont, E., Bourrier, V., and et al. (2018). Atmospheric reconnaissance of the habitable-zone Earth-sized planets orbiting TRAPPIST-1. *Nature Astronomy*, 2(3):214–219.

Dunn, R. J. H., Stanitski, D. M., Gobron, N., and Willett, K. M. (2020). Global Climate. In Rosenfeld, J., editor, *Bulletin of the American Meteorological Society*, volume 101, chapter 2, pages 9–128. American Meteorological Society.

Eggenberger, A. and Udry, S. (2010). Detection and Characterization of Extrasolar Planets through Doppler Spectroscopy. *EAS Publications Series*, 41:27–75.

exoplanet TEAM (2021). The Extrasolar Planets Encyclopaedia. `http://exoplanet.eu`. [Online; accessed 18-June-2021].

Gunell, H., Maggiolo, R., Nilsson, H., Stenberg Wieser, G., Slapak, R., Lindkvist, J., Hamrin, M., and De Keyser, J. (2018). Why an intrinsic magnetic field does not protect a planet against atmospheric escape. *A&A*, 614:L3.

Hartman, J. D., Bakos, G. A., Kovács, G., and Noyes, R. W. (2010). A large sample of photometric rotation periods for FGK Pleiades stars. *Monthly Notices of the Royal Astronomical Society*, 408(1):475–489.

Irwin, J., Aigrain, S., Bouvier, J., Hebb, L., Hodgkin, S., Irwin, M., and Moraux, E. (2009). The Monitor project: rotation periods of low-mass stars in M50. *Monthly Notices of the Royal Astronomical Society*, 392(4):1456–1466.

Irwin, J., Hodgkin, S., Aigrain, S., Hebb, L., Bouvier, J., Clarke, C., Moraux, E., and Bramich, D. M. (2007). The Monitor project: rotation of low-mass stars in the open cluster NGC 2516. *Monthly Notices of the Royal Astronomical Society*, 377(2):741–758.

Johnstone, C. P. (2021). Stellar winds and planetary atmospheres. *arXiv e-prints*, page arXiv:2105.11243.

Johnstone, C. P., Bartel, M., and Güdel, M. (2020). The active lives of stars: A complete description of the rotation and XUV evolution of F, G, K, and M dwarfs. *Astronomy & Astrophysics*, 649:A96.

Johnstone, C. P., Güdel, M., Lammer, H., and Kislyakova, K. G. (2018). The Upper Atmospheres of Terrestrial Planets: Carbon Dioxide Cooling and the Earth's Thermospheric Evolution. *Astronomy & Astrophysics*, 617.

Johnstone, C. P., Güdel, M., Stökl, A., Lammer, H., Tu, L., Kislyakova, K., Lüftinger, T., Odert, P., Erkaev, N., and Dorfi, E. (2015). The evolution of stellar rotation and the hydrogen atmospheres of habitable-zone terrestrial planets. *The Astrophysical Journal*, 815.

Johnstone, C. P., Khodachenko, M. L., Lüftinger, T., Kislyakova, K. G., Lammer, H., and Güdel, M. (2019). Extreme hydrodynamic losses of Earth-like atmospheres in the habitable zones of very active stars. *A&A*, 624:L10.

Johnstone, C. P., Lammer, H., Kislyakova, K. G., Scherf, M., and Güdel, M. (2021). The young Sun's XUV-activity as a constraint for lower CO2-limits in the Earth's Archean atmosphere. *Earth and Planetary Science Letters*, 576:117197.

Kasting, J. F., Whitmire, D. P., and Reynolds, R. T. (1993). Habitable Zones around Main Sequence Stars. *Icarus*, 101(1):108–128.

Kingma, D. P. and Ba, J. (2017). Adam: A Method for Stochastic Optimization.

Kislyakova, K. G., Johnstone, C. P., Odert, P., Erkaev, N. V., Lammer, H., Lüftinger, T., Holmström, M., Khodachenko, M. L., and Güdel, M. (2014). Stellar wind interaction and pick-up ion escape of the Kepler-11 "super-Earths". *A&A*, 562:A116.

Kopparapu, R. K., Ramirez, R., Kasting, J. F., Eymet, V., Robinson, T. D., Mahadevan, S., Terrien, R. C., Domagal-Goldman, S., Meadows, V., and Deshpande, R. (2013). HABITABLE ZONES AROUND MAIN-SEQUENCE STARS: NEW ESTIMATES. *The Astrophysical Journal*, 765(2):131.

Kubyshkina, D., Cubillos, P. E., Fossati, L., Erkaev, N. V., Johnstone, C. P., Kislyakova, K. G., Lammer, H., Lendl, M., Odert, P., and Güdel, M. (2019). Close-in Sub-Neptunes Reveal the Past Rotation History of Their Host Stars: Atmospheric Evolution of Planets in the HD 3167 and K2-32 Planetary Systems. *The Astrophysical Journal*, 879(1):26.

Lammer, H., Stökl, A., Erkaev, N. V., Dorfi, E. A., Odert, P., Güdel, M., Kulikov, Y. N., Kislyakova, K. G., and Leitzinger, M. (2014). Origin and loss of nebula-captured hydrogen envelopes from 'sub'- to 'super-Earths' in the habitable zone of Sun-like stars. *Monthly Notices of the Royal Astronomical Society*, 439(4):3225–3238.

Meibom, S., Mathieu, R. D., and Stassun, K. G. (2009). Stellar Rotation in M35: Mass-Period Relations, Spin-Down Rates, and Gyrochronology. *The Astrophysical Journal*, 695(1):679–694.

Nakazawa, K., Mizuno, H., Sekiya, M., and Hayashi, C. (1985). Structure of the primordial atmosphere surrounding the early-earth. *Journal of geomagnetism and geoelectricity*, 37(8):781–799.

Nielsen, M. A. (2015). *Neural Networks and Deep Learning*. Determination press.

Noack, L., Godolt, M., von Paris, P., Plesa, A.-C., Stracke, B., Breuer, D., and Rauer, H. (2014). Can the interior structure influence the habitability of a rocky planet? *Planetary and Space Science*, 98:14–29. Planetary evolution and life.

Owen, J. E. and Mohanty, S. (2016). Habitability of terrestrial-mass planets in the HZ of M Dwarfs – I. H/He-dominated atmospheres. *Monthly Notices of the Royal Astronomical Society*, 459(4):4088–4108.

Peek, J. E. G., Jones, C. K., and Hargis, J. (2020). Convolutional Neural Networks in Astronomy, and Applications for Diffuse Structure Discovery. In Ballester, P., Ibsen, J., Solar, M., and Shortridge, K., editors, *Astronomical Data Analysis Software and Systems XXVII*, volume 522 of *Astronomical Society of the Pacific Conference Series*, page 381.

Qian, L., Burns, A. G., Solomon, S. C., and Wang, W. (2017). Carbon dioxide trends in the mesosphere and lower thermosphere. *Journal of Geophysical Research: Space Physics*, 122:4474–4488.

Ramachandran, P., Zoph, B., and Le, Q. V. (2017). Searching for Activation Functions.

Rebull, L. M., Stauffer, J. R., Bouvier, J., Cody, A. M., Hillenbrand, L. A., Soderblom, D. R., Valenti, J., Barrado, D., Bouy, H., Ciardi, D., Pinsonneault, M., Stassun, K., Micela, G., Aigrain, S., Vrba, F., Somers, G., Christiansen, J., Gillen, E., and Cameron, A. C. (2016). ROTATION IN THE PLEIADES WITH K2. I. DATA AND FIRST RESULTS. *The Astronomical Journal*, 152(5):113.

Reiners, A., Schüssler, M., and Passegger, V. M. (2014). Generalized Investigation of the Rotation-Activity Relation: Favoring Rotation Period instead of Rossby Number. *The Astrophysical Journal*, 794(2):144.

Reinhold, T., Shapiro, A. I., Solanki, S. K., Montet, B. T., Krivova, N. A., Cameron, R. H., and Amazo-Gómez, E. M. (2020). The Sun is less active than other solar-like stars. *Science*, 368(6490):518–521.

Ribas, I., Guinan, E. F., Güdel, M., and Audard, M. (2005). Evolution of the Solar Activity over Time and Effects on Planetary Atmospheres. I. High-Energy Irradiances (1-1700 Å). *The Astrophysical Journal*, 622:680–694.

Schmitt, J. H. M. M., Fleming, T. A., and Giampapa, M. S. (1995). The X-Ray View of the Low-Mass Stars in the Solar Neighborhood. *The Astrophysical Journal*, 450:392.

Spada, F., Demarque, P., Kim, Y. C., and Sills, A. (2013). The Radius Discrepancy in Low-mass Stars: Single versus Binaries. *The Astrophysical Journal*, 776(2):87.

Stern, R. A., Schmitt, J. H. M. M., and Kahabka, P. T. (1995). ROSAT All-Sky Survey Observations of the Hyades Cluster. *The Astrophysical Journal*, 448:683.

Stökl, A., Dorfi, E., and Lammer, H. (2015). Hydrodynamic simulations of captured protoatmospheres around Earth-like planets. *A&A*, 576:A87.

Tian, F. (2013). Conservation of total escape from hydrodynamic planetary atmospheres. *Earth and Planetary Science Letters*, 379:104–107.

Tian, F., Kasting, J. F., Liu, H.-L., and Roble, R. G. (2008). Hydrodynamic planetary thermosphere model: 1. Response of the Earth's thermosphere to extreme solar EUV conditions and the significance of adiabatic cooling. *Journal of Geophysical Research (Planets)*, 113(E5):E05008.

Tsiaras, A., Rocchetto, M., Waldmann, I. P., Venot, O., Varley, R., Morello, G., Damiano, M., Tinetti, G., Barton, E. J., Yurchenko, S. N., and Tennyson, J. (2016). DETECTION OF AN ATMOSPHERE AROUND THE SUPER-EARTH 55 CANCRI e. *The Astrophysical Journal*, 820(2):99.

Tsiaras, A., Waldmann, I. P., Tinetti, G., Tennyson, J., and Yurchenko, S. N. (2019). Water vapour in the atmosphere of the habitable-zone eight-Earth-mass planet K2-18 b. *Nature Astronomy*, 3(12):1086–1091.

Tu, L., Johnstone, C. P., Güdel, M., and Lammer, H. (2015). The extreme ultraviolet and X-ray Sun in Time: High-energy evolutionary tracks of a solar-like star. *A&A*, 577:L3.

Tuomi, M., Jones, H. R. A., Butler, R. P., Arriagada, P., Vogt, S. S., Burt, J., Laughlin, G., Holden, B., Shectman, S. A., Crane, J. D., Thompson, I., Keiser, S., Jenkins, J. S., Berdiñas, Z., Diaz, M., Kiraga, M., and Barnes, J. R. (2019). Frequency of planets orbiting M dwarfs in the Solar neighbourhood.

Wolfgang, A. and Lopez, E. (2015). How Rocky Are They? The Composition Distribution of Kepler's Sub-Neptune Planet Candidates within 0.15 AU. *The Astrophysical Journal*, 806(2):183.